

1 **Sensitivity of aerosol and cloud properties to coupling strength of**
2 **marine boundary layer clouds over the northwest Atlantic**

3 Kira Zeider¹, Kayla McCauley²⁺, Sanja Dmitrovic³, Leong Wai Siu², Yonghoon Choi^{4,5}, Ewan C.
4 Crosbie^{4,5}, Joshua P. DiGangi⁴, Glenn S. Diskin⁴, Simon Kirschler^{6,7}, John B. Nowak⁴, Michael
5 A. Shook⁴, Kenneth L. Thornhill^{4,5}, Christiane Voigt^{6,7}, Edward L. Winstead^{4,5}, Luke D. Ziemba⁴,
6 Paquita Zuidema⁸, Armin Sorooshian^{1,2,3*}

7 ¹Department of Chemical and Environmental Engineering, University of Arizona, Tucson, AZ, 85721, USA

8 ²Department of Hydrology and Atmospheric Sciences, University of Arizona, Tucson, AZ, 85721, USA

9 ³James C. Wyant College of Optical Sciences, University of Arizona, Tucson, AZ 85721, USA

10 ⁴NASA Langley Research Center, Hampton, VA, 23681, USA

11 ⁵Analytical Mechanics Associates, Hampton, VA, 23666, USA

12 ⁶Institute of Atmospheric Physics, German Aerospace Center, Germany

13 ⁷Institute of Atmospheric Physics, University Mainz, Germany

14 ⁸Rosenstiel School of Marine, Atmospheric, and Earth Science, University of Miami, Miami, FL

15 ⁺Now at EPA, Research Triangle Park, NC 27711

16

17 **Correspondence to:* Armin Sorooshian (armin@arizona.edu)

18 **Abstract**

19 Quantifying the degree of coupling between marine boundary layer clouds and the surface is critical for understanding
20 the evolution of low clouds and explaining the vertical distribution of aerosols and microphysical cloud properties.
21 ~~Previous work has characterized the boundary layer as either coupled or decoupled, but this study rather considers four~~
22 ~~degrees of coupling, ranging from strongly to weakly coupled.~~ We use aircraft data from the NASA Aerosol Cloud
23 meTeorology Interactions oVer western ATlantic Experiment (ACTIVATE) to assess aerosol and cloud characteristics
24 for the following four regimes, quantified using differences in liquid water potential temperature (θ_e) and total water
25 mixing ratio (q_t) between ~~flight data~~ near-surface level (~150 m) and directly below cloud bases: strong coupling ($\Delta\theta_e$
26 ≤ 1.0 K, $\Delta q_t \leq 0.8$ g kg⁻¹), moderate coupling with high $\Delta\theta_e$ ($\Delta\theta_e > 1.0$ K, $\Delta q_t \leq 0.8$ g kg⁻¹), moderate coupling with
27 high Δq_t ($\Delta\theta_e \leq 1.0$ K, $\Delta q_t > 0.8$ g kg⁻¹), weak coupling ($\Delta\theta_e > 1.0$ K, $\Delta q_t > 0.8$ g kg⁻¹). Results show that (i) turbulence
28 is greater in the strong coupling regime compared to the weak coupling regime, with the former corresponding to ~~more~~
29 ~~vertical homogeneity~~ in 550 nm aerosol scattering, integrated aerosol volume concentration, and giant aerosol number
30 concentration ($D_p > 3$ μ m), coincident with increased MBL mixing; (ii) cloud drop number concentration is greater
31 during periods of strong coupling due to the greater upward vertical velocity and subsequent activation of particles;
32 (iii) sea-salt tracer species (Na^+ , Cl^- , Mg^{2+} , K^+) are present in greater concentrations in the strong coupling regime
33 compared to weak coupling, while tracers of continental pollution (Ca^{2+} , ~~nss-SO₄²⁻~~, NO_3^- , oxalate, and NH_4^+) are
34 higher in mass fraction for the weak coupling regime. Additionally, pH and $\text{Cl}^-:\text{Na}^+$ (a marker for chloride depletion)
35 are consistently lower in the weak coupling regime. There were ~~also~~ differences between the two moderate regimes:
36 the moderate, high Δq_t regime had greater turbulent mixing and sea salt concentrations in cloud water, along with
37 smaller differences in integrated volume and giant aerosol number concentration ~~across~~ the two vertical levels
38 ~~compared~~. This work shows value in defining multiple coupling regimes (rather than the traditional coupled versus
39 decoupled) and demonstrates differences in aerosol and cloud behavior in the MBL for the various regimes.

40

- Deleted: , however
- Deleted: uses
- Deleted: In this study, w
- Deleted: of coupling strength as
- Deleted: θ_e
- Deleted: a
- Deleted: θ_e
- Deleted: θ_e
- Deleted: θ_e
- Deleted: θ_e
- Deleted: θ_e
- Deleted: smaller differences
- Deleted: between the near-surface level and just below marine boundary layer (MBL) cloud bases
- Deleted: ,
- Deleted: ,
- Deleted: Ca^{2+} , nss-SO₄²⁻, NO_3^- , oxalate, and NH_4^+ (
- Deleted:)
- Formatted: Not Superscript/ Subscript
- Deleted: between
- Deleted: compared

61 **1 Introduction**

62 The composition of marine boundary layer (MBL) cloud properties is strongly linked to the lower troposphere's
 63 vertical structure, making it critical to understand the degree of coupling between boundary layer clouds and the
 64 ocean's surface. When the MBL is well-mixed, there is a thermodynamic exchange between the ocean's surface and
 65 the cloud deck, and it is considered coupled. A decoupled MBL is characterized by a stable layer separating two well-
 66 mixed layers (the cloud deck and sub-cloud layer), preventing exchange between the ocean's surface and the cloud
 67 base (Nicholls, 1984; Dong et al., 2015; Jones et al., 2011; Wang et al., 2016). Whether the MBL cloud deck is coupled
 68 or decoupled to the surface has potentially important implications for cloud and aerosol properties (Dong et al., 2015;
 69 Wang et al., 2016; Griesche et al., 2021), radiative forcing (Goren et al., 2018), and precipitation (Bretherton et al.,
 70 2010; Dong et al., 2015). Changes in cloud properties and precipitation affect how much solar radiation is reflected to
 71 space (Twomey, 1974; Albrecht, 1989), which in turn affects how much radiative cooling occurs (Ramanathan et al.,
 72 1989).

73
 74 Past studies have investigated coupling behavior of marine stratocumulus due to their relatively high frequency over
 75 the ocean's surface and strong impact on the Earth's radiation budget (Zuidema et al., 2009; Jones et al., 2011; Dong
 76 et al., 2015; Wang et al., 2016; Goren et al., 2018). In marine regions, well-mixed moist thermodynamic statistics
 77 indicate coupling of the sub-cloud layer to the surface (Bretherton et al., 1997; Jones et al., 2011; Dong et al., 2015;
 78 Wang et al., 2016; Su et al., 2022). Studies beyond those previously mentioned over the southeast and northeast Pacific
 79 have applied these methods to other regions, such as the Arctic (Griesche et al., 2021) and over land in the Southern
 80 Great Plains of the United States (Su et al., 2022). Table 1 provides a synthesis of previous studies that utilized
 81 thermodynamic statistics for determining coupling, including criteria used, the region in which the study was
 82 conducted, and the cloud types investigated.

83
 84 **Table 1: Summary of coupling criteria and regional conditions from previous work in comparison to this study.**

Study region; reference	Criteria	Secondary criteria	Layers used	Cloud type
Southeast Pacific; Jones et al. (2011)	Coupled: $\Delta q_t < 0.5 \text{ g kg}^{-1}$ & $\Delta \theta_t < 0.5 \text{ K}$	Coupled: distance between lifting condensation level (LCL) and cloud base is < 150 m Decoupled: distance > 150 m	Bottom 25% of surface layer to cloud base height	Marine strato- cumulus
Azores (Graciosa Island; Northeast Atlantic); Dong et al. (2015)	All other profiles are considered decoupled			
Northeast Pacific; Wang et al. (2016)	Decoupled: $\Delta q_t > 0.6 \text{ g kg}^{-1}$ & $\Delta \theta_t > 1.0 \text{ K}$ All other clouds are considered coupled	N/A		

Southern Great Plains (U.S.); Su et al. (2022)	Coupled: $\Delta\theta_\ell < 1.0$ K Decoupled: $\Delta\theta_\ell > 1.0$ K			Different Thermodynamic Stability (DTDS) method	Cloud base height minus planetary boundary layer height	Low clouds over land, specifically cumulus
Northwest Atlantic; This Study	Degree	Δq_ℓ	$\Delta\theta_\ell$	N/A	Below cloud base leg (~100 m below base) minus MinAlt leg (avg. alt ~150 m)	Marine clouds spanning continuum from stratiform to cumulus
	Strong	$\leq 0.8 \text{ g kg}^{-1}$	$\leq 1.0 \text{ K}$			
	Moderate, high $\Delta\theta_\ell$	$\leq 0.8 \text{ g kg}^{-1}$	$> 1.0 \text{ K}$			
	Moderate, high Δq_ℓ	$> 0.8 \text{ g kg}^{-1}$	$\leq 1.0 \text{ K}$			
Weak	$> 0.8 \text{ g kg}^{-1}$	$> 1.0 \text{ K}$				

85
86 As over 45% of the ocean's surface is covered by MBL clouds (Warren et al., 1988), examining relations between
87 aerosol and cloud characteristics with coupling strength is important. Investigation of coupling behavior has not yet
88 been carried out for the northwest Atlantic region, which is a complex thermodynamic region for such work as it is
89 not a classical sub-tropical zone with a stratocumulus cloud deck like most regions investigated in Table 1 (Painemal
90 et al., 2021, 2023). The synoptic conditions over the northwest Atlantic are such that the wintertime has higher cloud
91 fraction with more influence from stratiform boundary layer clouds, whereas the summertime has more trans-Atlantic
92 flow in addition to lower cloud fraction with higher sea surface temperatures promoting shallow cumulus clouds
93 (Painemal et al., 2021). During winter, there is more offshore advection of continental air (Corral et al., 2021;
94 Dadashazar et al., 2021), enhanced precipitation frequency (Painemal et al., 2021), and cold air outbreaks (CAOs), in
95 which cold air is advected across the Gulf Stream front resulting in pronounced differences between air and sea surface
96 temperatures (Brümmer, 1997; Papritz & Spengler, 2015; Seethala et al., 2021). CAOs are typically associated with
97 strong turbulent mixing, leading to the deepening of the boundary layer (Dadashazar et al., 2021; Painemal et al.,
98 2021; Papritz & Spengler, 2015; Tornow et al., 2022). During CAO events, surface wind convergence is driven by
99 horizontal pressure and boundary layer height gradients, contributing to a statically unstable **lower** troposphere
100 (Painemal et al., 2021; Seethala et al., 2021).

101
102 Motivated by meteorological differences between the northwest Atlantic and other regions in Table 1, the question
103 arises as to whether it is restrictive to consider just the categories of coupled and decoupled clouds; instead, it may be
104 instructive to consider more categories and that they all may have some degree of coupling ranging from weak to
105 strong. This strategy is built off past reports suggesting that the use of the term "decoupled" may not be appropriate
106 and that an MBL can be coupled even though it is poorly mixed (Stevens et al., 1998). The latter case can be viewed
107 as weakly coupled due to episodic updraft-driven convection that is less efficient at mixing the MBL than is the case
108 in well-mixed MBLs in which downdrafts associated with cloud-top radiative cooling couple the cloud and sub-cloud
109 layers (Stevens et al., 1998). Thus, the perspective we embrace in this work is that low-level clouds (< 2 km) can be
110 viewed as always being coupled to sub-cloud layers but to varying degrees.

111

Deleted: (Stevens et al., 1998)

113 The goal of this study is to leverage an opportune aircraft dataset covering multiple seasons between 2020 to 2022
114 from NASA's Aerosol Cloud Meteorology Interactions over the western Atlantic Experiment (ACTIVATE;
115 Sorooshian et al., 2019) to quantify the frequency of occurrence for four different coupling regimes and how aerosol
116 and cloud characteristics vary between them. We emphasize that this study is different in nature to those in Table 1 in
117 that we do not examine as rigorously the vertical extent of the full cloudy boundary layer but instead focus more on
118 aerosol and cloud characteristics for different coupling regimes based on definitions limited to the vertical region
119 below cloud bases. The analyses presented here are important for reasons such as knowing how well the aerosol near
120 the surface level represent the aerosol just below cloud bases, with implications for the aerosol that largely govern the
121 drop concentration budget. In Sect. 2 we summarize the measurements and methods, including criteria applied with
122 traditionally used thermodynamic variables to differentiate between four coupling categories. In Sect. 3 we report
123 results including the frequency of occurrence of the four coupling regimes, and differences in aerosol properties (light
124 scattering, number/volume concentration) and cloud microphysical properties (composition and droplet number
125 concentration) between these categories to see how they compare to past studies for other regions. Although there are
126 scarce previous reports of such findings (e.g., Dong et al., 2015; Wang et al., 2016), the central hypotheses are based
127 on confirming what has been shown or implied in other regions, in that more strongly coupled cases will have (i) more
128 vertical homogeneity in aerosol properties between the sub-cloud layer and closer to the ocean's surface, (ii) cloud
129 composition reflecting significantly more sea salt influence (Wang et al., 2016), and (iii) higher cloud drop number
130 concentration, compared to weakly coupled cases (Dong et al., 2015). Differences identified in aerosol and cloud
131 characteristics between these four coupling regimes are important to inform both future flight designs and data analysis
132 research to account for thermodynamic profiles when examining aspects of aerosol and cloud microphysics when
133 using either satellite, reanalysis, airborne, or ground-based datasets.

134

135 2 Data and Methodology

136 2.1 Overview of ACTIVATE

137 ACTIVATE was largely based out of NASA Langley Research Center in Hampton, Virginia and carried out research
138 flights (RFs) with two spatially coordinated aircraft as part of six deployments in winter and summer months between
139 2020 and 2022, with extensive measurement and deployment details provided elsewhere (Sorooshian et al., 2023).
140 Secondary bases were used for a subset of flights in 2022, including in Bermuda for June 2022. Winter and summer
141 are broadly defined as including the months of November-April and May-September, respectively. The HU-25 Falcon
142 flew level legs in, below, and above MBL clouds to collect in-situ atmospheric state, aerosol, trace gas, and cloud
143 measurements, while the high-flying King Air at ~9 km launched dropsondes and carried out remote sensing. The
144 focus of this work is data collected by the Falcon. Out of 179 total flights, 135 were used that offered data conducive
145 to this study's analysis including having the Falcon conduct "statistical survey" flights with "cloud ensembles" (Fig.
146 1), along with several physical conditions satisfied as discussed in Sect. 2.5. During statistical survey flights, which
147 accounted for 93% of ACTIVATE's flights, the Falcon repeatedly flew a series of legs with Fig. 1 visually depicting
148 one such cloud ensemble whereby the plane flew the following legs in this nominal order: two pairs of legs below
149 cloud base (BCB) and above cloud base (ACB) followed by a descent to the minimum altitude (MinAlt) possible

Deleted: ts

Deleted: aerosol

Deleted: :

Deleted: similar values for aerosol and atmospheric properties (such as aerosol number and concentration) in the

Deleted: compared to

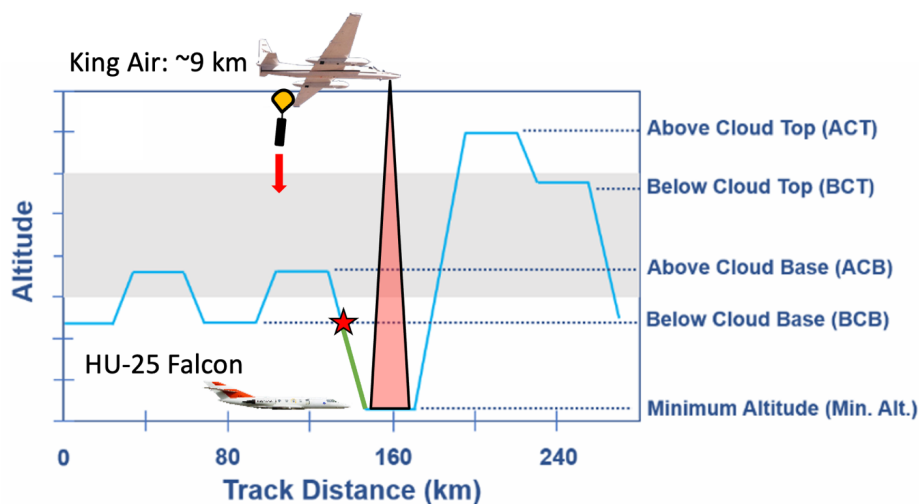
Deleted: ;

Deleted: ;

Deleted: the M

159 (~150 m above sea level) and then a subsequent slant ascent for a leg above cloud top (ACT) followed by a final leg
 160 below cloud top (BCT). Separate ensembles flown in clear air conditions are outside the scope of this work. Each leg
 161 duration was ~3.3 minutes (equivalent to ~ 24 km) with the Falcon flying at ~120 m s⁻¹ (Dadashazar et al., 2022a).
 162 The vertical slant ascents/descents between level legs especially down to MinAlt and up to ACT were helpful in
 163 gathering vertically-resolved information during ensembles.

164



165

166 Figure 1: Cloudy ensemble flight strategy of the HU-25 Falcon during the ACTIVATE flights, where the grey box represents
 167 a typical cloud layer with upper and lower boundaries representing cloud top and base, respectively. The order of legs was
 168 the nominal plan that was flown, but sometimes the legs were flown in a different order based on flight restrictions and
 169 cloud conditions. The red star indicates where the BCB level would be marked for this particular flight pattern, which is
 170 during the slant descent from ACB to MinAlt and uses the mean altitude of the preceding BCB leg immediately before the
 171 ACB leg; that level would then be compared to the adjacent MinAlt level that begins at the end of the slant descent.
 172 Otherwise, MinAlt-BCB pairs that are used include when a MinAlt level leg was immediately preceded or succeeded by a
 173 BCB level leg. The green line illustrates the data that would be used to investigate the vertical structure of the layer, starting
 174 with the last timestamp from the pseudo-BCB leg and ending with the first timestamp in the MinAlt leg.

175

176 2.2 Implementation of Flight Legs

177 Across ACTIVATE's six deployments, MinAlt and BCB legs were identified for RFs when the Falcon flew cloud
 178 ensembles (Fig. 1). There were several instances when the MinAlt and BCB legs were not immediately adjacent and
 179 separated by another leg, such as at ACB (i.e., the flight order was BCB-ACB-MinAlt; Fig. 1). In those cases, to get
 180 MinAlt/BCB pairs that were closer in time, our method involved identifying the BCB altitude during the slant
 181 altitudinal change (either descent or ascent) between MinAlt-ACB based on the altitude of the BCB leg immediately
 182 before the ACB leg (see red star in Fig. 1). A secondary check was made to ensure that identified BCB leg was below

184 cloud base using 1-Hz LWC and N_d values from the FCDP (criteria in Sect. 2.5). The vertical structure of the layer
 185 between MinAlt and BCB was examined using data between the last time stamp in the MinAlt/BCB leg (i.e.,
 186 whichever was first in the MinAlt-BCB pair) and first-time stamp in the subsequent BCB/MinAlt leg (i.e., whichever
 187 was second in the MinAlt-BCB pair). This is indicated by a green line on Fig. 1, which begins with the last time stamp
 188 from the pseudo-BCB leg (indicated by the red star) and ends with the first time stamp in the MinAlt leg. For
 189 simplicity, we refer to the case of using BCB data during slant profiles as “legs” too, even though they were not level
 190 legs. This study compares various measurement data (Sect. 2.5) between MinAlt and BCB legs using the last/first 5
 191 seconds of data during adjacent MinAlt-BCB legs, and in the case of slants, we use the 2 points before and after the
 192 actual BCB point (the red star in Fig. 1) for a total of 5 points, (average altitude range ~ 20 m), that represent the BCB
 193 level with the condition that all data were out of cloud.

194

195 2.3 Instrumentation

196 A summary of instrumentation relevant to this study is shown in Table 2 and briefly described here. A nephelometer
 197 (TSI-3563) measured the dry scattering coefficient at 550 nm (particle diameter (D_p) < 5.0 μm for 2020 and D_p < 1.0
 198 μm for 2021 and 2022); a Laser Aerosol Spectrometer (LAS; TSI-3340) measured aerosol size distributions (0.1 μm
 199 < D_p < 5.0 μm) and here we use the integrated aerosol volume concentration data; a Fast Cloud Droplet Probe (FCDP;
 200 SPEC Inc.) measured liquid water content (LWC) and particle and cloud drop size distributions between 3 and 50 μm ;
 201 a two-dimensional stereo (2D-S; SPEC Inc.; 25 μm < D_p < 1500 μm) probe provided LWC, liquid droplet effective
 202 diameter, and an ice flag, where the ice flag is equal to 1 if ice was detected (otherwise the variable is equal to 0); a
 203 diode laser hygrometer (DLH) measured the water vapor mixing ratio (q_w); a turbulent air motion measurement system
 204 (TAMMS) measured three-dimensional winds (Thornhill et al., 2003); and an axial cyclone cloud water collector
 205 (AC3) (Crosbie et al., 2018) collected cloud water samples by inertially separating droplets from the air stream.
 206 Collected cloud water samples were then analyzed post-flight with ion chromatography (IC) with operating conditions
 207 summarized elsewhere (Corral et al., 2022; Gonzalez et al., 2022). Section 2.6 describes the cloud water data in more
 208 detail.

209

210 **Table 2: Summary of field campaign instrumentation used and corresponding measurements.**

Instruments	Measurements	Diameter (μm)	Reference
TSI-3563 Nephelometer	Dry scattering coefficient at 550 nm	< 5.0 for 2020; < 1.0 for 2021 & 2022	Ziemba et al. (2013)
TSI-3340 Laser Aerosol Spectrometer (LAS)	Integrated aerosol volume concentration	0.1 – 5.0	Froyd et al. (2019)
SPEC Inc. Fast Cloud Droplet Probe (FCDP)	Liquid water content (LWC), particle number concentration (N_a), cloud drop number concentration (N_d)	3 – 50	Kirschler et al. (2022)

Deleted: ;

Deleted:

Deleted: to

SPEC Inc. Two-Dimensional Stereo Probe, Horizontal Arm (2DS-H)	LWC, effective diameter for liquid, ice flag	25 – 1500	Kirschler et al. (2023)
Diode Laser Hygrometer (DLH)	Water vapor mixing ratio (q_v)	N/A	Diskin et al. (2002)
Axial Cloud Water Collector (AC3)	Cloud water composition	see Sect. 2.6	Crosbie et al. (2018)
Turbulent Air Motion Measurement System (TAMMS)	Three dimensional winds	N/A	Thornhill et al. (2003)

214

215

216 2.4 Marine Boundary Layer Coupling

217 2.4.1 Thermodynamic Variables

218 To estimate the degree of coupling within the marine boundary layer, we consider the change in vertical profile of two
219 parameters: total water mixing ratio (q_t) and liquid water potential temperature (θ_t). Relevant to this study are these
220 equations,

221

$$222 q_\ell = \frac{LWC}{\rho_d} \quad (1)$$

223

$$224 q_t = q_v + q_\ell \quad (2)$$

225

226 where the total water mixing ratio is the sum of water vapor mixing ratio (q_v) and liquid water mixing ratio (q_ℓ). The
227 water vapor mixing ratio (q_v) provided by the DLH is converted from ppmv to g kg^{-1} . The liquid water mixing ratio
228 (q_ℓ) is defined as the ratio of the mass of liquid water to the mass of dry air within a unit volume of air, which is
229 equivalent to the ratio of LWC (provided by the FCDP) and the density of dry air (ρ_d).

230 Also relevant are these equations,

231

$$232 \theta = (T + 273.15) \times \left(\frac{p_0}{p}\right)^\kappa \quad (3)$$

233

$$234 \theta_\ell = \theta - \left(\frac{L_v}{c_{pd}}\right) \times q_\ell \quad (4)$$

235

236 where in equation 3, T and p are the given temperature in $^\circ\text{C}$ and pressure in hPa from Falcon measurements,
237 respectively, p_0 is the reference pressure (= 1000 hPa), and κ is the ratio of gas constant of dry air (R_d) to the specific
238 heat of dry air at constant pressure (c_{pd}). In equation 4, L_v is latent heat of vaporization and c_{pd} is the specific heat of

Deleted: kappa

240 dry air at constant pressure. When LWC is equal to 0, θ_t is equal to θ . θ_t is useful for the purposes of this study as it
241 is not significantly influenced by evaporating precipitation. Information regarding LWC thresholds for MinAlt-BCB
242 pairs is included in Sect. 2.5.

243
244 For each MinAlt and BCB leg, the average θ_t and q_t across the leg was calculated and the difference between the two
245 layers was taken as follows:

$$246 \Delta q_t = q_{t,MinAlt} - q_{t,BCB^*} \quad (5)$$

$$247 \Delta \theta_t = \theta_{t,BCB^*} - \theta_{t,MinAlt} \quad (6)$$

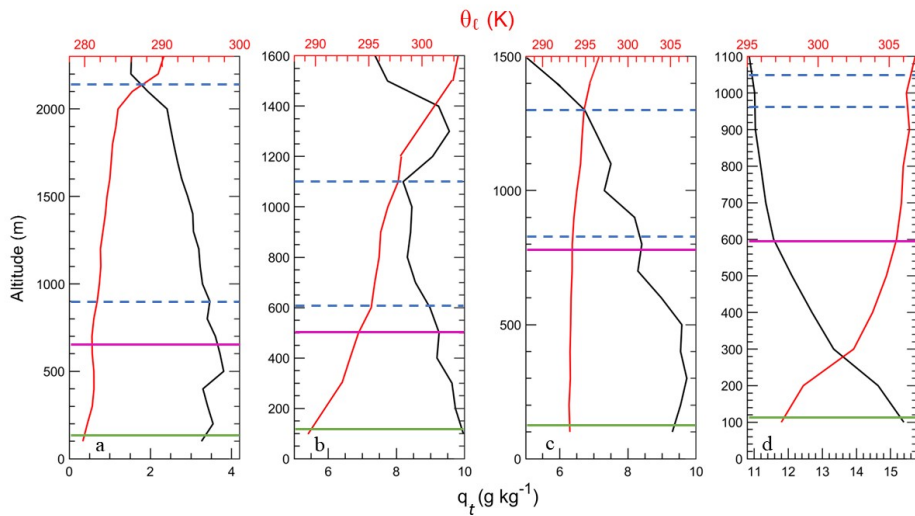
248
249 where in both equations 5-6, the order of legs on the right-hand side is meant to arrive at a positive value for the
250 difference based on expectation.

251 252 253 **2.4.2 Coupling Criteria**

254 The criteria we use for the different coupling regimes were informed by (but are not identical to) those used in past
255 work (Jones et al., 2011; Dong et al., 2015; Wang et al., 2016; Su et al., 2022). Our focus was on comparing the vertical
256 range between MinAlt and BCB legs due to the focus on examining aerosol characteristics in particular within that
257 range and also cloud microphysical conditions above cloud base. To qualify as strongly coupled, the difference
258 between MinAlt and BCB had to satisfy these conditions: $\Delta q_t \leq 0.8 \text{ g kg}^{-1}$ and $\Delta \theta_t \leq 1.0 \text{ K}$ (example in Fig. 2a). Since
259 Δq_t is more influenced by evaporation and condensation, whereas $\Delta \theta_t$ is more affected by air mass mixing (such as
260 entrainment) and diabatic heating and cooling, it is proposed to have two degrees of moderate coupling – when one
261 of Δq_t and $\Delta \theta_t$ fit the strong coupling criteria and the other did not (Fig. 2b-c). Finally, profiles are considered “weakly
262 coupled” when both Δq_t and $\Delta \theta_t$ do not satisfy the strong coupling criteria values (Fig. 2d). Vertical profiles of q_t and
263 θ_t were examined for all MinAlt/BCB pairs to ensure robustness of the categorization method. [We note that while Fig.
264 2a/d show BCB legs being relatively farther below the actual cloud base height \(Fig. 2a = 223 m; Fig. 2d = 370 m\)
265 than the other two examples \(Fig. 2b = 101 m; Fig. 2c = 30 m\), the former two were anomalous cases and usually the
266 BCB legs were closer to cloud base. As noted by Dadashazar et al. \(2022b\), the Falcon aimed to conduct BCB and
267 ACB legs about ~100 m below and above the estimated cloud base height, respectively. Median/mean distances from
268 BCB to cloud bases were as follows for all samples in the four coupling categories: strong = 73/87 m; moderate, high
269 \$\Delta \theta_t = 101/119 \text{ m}\$; moderate, high \$\Delta q_t = 69/71 \text{ m}\$; weak = 104/142 m. The use of the two moderate categories is
270 exploratory in nature and meant to identify if differences are found between both themselves and the more extreme
271 categories of strong and weak. Appendix A further explores differences between the two moderate regimes and
272 suggests that the moderately coupled category with high \$\Delta \theta_t\$ is influenced more by processes above the MBL such as
273 entrainment of dry air with high potential temperature whereas the other moderate category with high \$\Delta q_t\$ is influenced
274 by surface processes.](#)

Formatted: Subscript

Formatted: Subscript



276
 277 **Figure 2: Representative vertical profiles of θ_t and q_t for (a) strong coupling from RF 44 on 3 February 2021, (b) moderate**
 278 **coupling with high $\Delta\theta_t$ from RF 150 on 5 May 2022, (c) moderate coupling with high Δq_t from RF 66 on 18 May 2021, and**
 279 **weak coupling from RF 158 on 20 May 2022. The dashed blue lines demarcate the cloud top and base levels, the magenta**
 280 **line indicates the BCB leg, and the green line indicates the MinAlt leg. There was a total of 411 MinAlt-BCB pairs analyzed**
 281 **in this study.**

282

283 2.5 Aerosol and Atmospheric Properties

284 There were several aerosol and atmospheric properties investigated in this study: aerosol scattering (scat) at 550 nm
 285 ($< 5 \mu\text{m}$ in 2020 and $< 1 \mu\text{m}$ in 2021-2022), integrated volume concentration (IntV: $0.1 < D_p < 5 \mu\text{m}$), particle number
 286 concentration (N_a ; $3 < D_p < 50 \mu\text{m}$), cloud drop number concentration (N_d ; $3 < D_p < 50 \mu\text{m}$), and turbulence (σ_w). Note
 287 that the N_a measurement from the FCDP for diameter $> 3 \mu\text{m}$ is important in this study to better isolate sea salt particles
 288 (Gonzalez et al., 2022). The integrated volume concentration also is expected to be influenced by larger sea salt
 289 particles in the measurement size range. These properties were averaged across each MinAlt and BCB pair and the
 290 difference between the MinAlt and BCB values was computed. To account for interference from cloud droplet shatter
 291 with the aerosol statistics, we only looked at MinAlt-BCB pairs when the sampling area was devoid of cloud, rain,
 292 and ice. The following three criteria had to be met: (1) ice flag from 2DS-H = 0, (2) effective liquid diameter from
 293 2DS-H $< 60 \mu\text{m}$, and (3) LWC from FCDP $< 0.005 \text{ g m}^{-3}$, to filter out conditions with ice, liquid precipitation, and
 294 clouds, respectively. When considering in-cloud conditions for N_d , additional criteria were needed based on FCDP
 295 data: LWC $> 0.05 \text{ g m}^{-3}$ and $N_d > 10 \text{ cm}^{-3}$ (Kirschler et al., 2023). N_d data was collected from ACB legs closest in
 296 proximity to a MinAlt-BCB pair ($< 30 \text{ min}$; 60% within 10 min) due to one of the study objectives being to examine
 297 how N_d varies between the four defined coupling regimes. Turbulence was calculated as the standard deviation of the
 298 vertical wind velocity for a level leg as done in other work (e.g., MacDonald et al., 2020).

Deleted: ¶

Deleted: 5

Deleted: s

Deleted: atmospheric conditions for each leg

303

304 2.6 Cloud Water Species

305 The nine cloud water species of interest in this study include non-sea salt calcium (nss-Ca²⁺), chloride (Cl⁻), potassium
306 (K⁺), magnesium (Mg²⁺), sodium (Na⁺), ammonium (NH₄⁺), nitrate (NO₃⁻), oxalate, and non-sea salt sulfate (nss-
307 SO₄²⁻). Calculations of nss-Ca²⁺ and nss-SO₄²⁻ utilized mass ratios and concentrations of pure Ca²⁺, Na⁺, and SO₄²⁻,
308 following the methodology outlined in Sect. 2.7 of AzadiAghdam et al. (2019). The IC is used to obtain concentrations
309 of cloud water species in aqueous units (mg L⁻¹), which were then converted to air equivalent concentrations using the
310 methods described in Gonzalez et al. (2022). Briefly, the cloud water sample was considered in-cloud under the criteria
311 LWC_{FCDP} > 0.05 g m⁻³. When this condition was met, the concentration was multiplied by the average LWC_{FCDP}
312 measured across the sampling time and divided by the density of water and ultimately converted to µg m⁻³ for the air
313 equivalent concentration. These units allow one to compare concentrations more fairly between samples to remove
314 biases due to varying amounts of water in different clouds. As cloud water samples were collected periodically during
315 flights, samples were only examined when a MinAlt or BCB leg being investigated was within 30 minutes or
316 overlapped with the collection period. Out of a total of 535 cloud water samples over the 6 deployments, 67 met the
317 criteria to be used for this study's MinAlt/BCB pairs. Statistics including mean, standard deviation (std. dev.),
318 minimum, maximum, and quartile ranges were calculated across the 67 data points for all nine cloud water species.

319

320 Additionally, cumulative average cloud water mass concentrations and mass fractions were calculated for the 67
321 samples. The total mass concentration for each coupling regime was found by the summation of only the nine chemical
322 species investigated in this manuscript. Welch's t-test calculations were conducted to compare the mean concentrations
323 of the investigated chemical species across coupling regimes. These tests were done in lieu of the traditional t-test due
324 to the assumption that the data used have unequal variances and thus are slightly more robust.

325

326 3 Results and Discussion

327 3.1 Thermodynamic Criteria

328 This section discusses the application of the developed thermodynamic criteria across all MinAlt-BCB pairs. In total,
329 411 MinAlt-BCB pairs were investigated (pair locations shown in Fig. 3), with the breakdown of the distribution
330 across the different degrees of coupling shown in Fig. 3 and 4. The majority of the pairs were classified as strongly
331 coupled, with a breakdown of 71% (strongly coupled), 14% (moderately coupled with high Δθ_l), 10% (moderately
332 coupled with high Δq_l), and 5% (weakly coupled). Strong turbulent mixing in the northwest Atlantic Ocean, especially
333 during the winter (Brunke et al., 2022) which is when most pairs were identified, is likely why the majority of pairs
334 were found to be strongly coupled, as the coupling parameters θ_l and q_l are relatively constant vertically from the
335 surface to near cloud bases due to the strong mixing (Fig. 2a).

336

337 There are no major spatial distribution differences for MinAlt-BCB pairs across the four coupling regimes with minor
338 exceptions being that the majority of pairs identified farther offshore around Bermuda were for both the strongly
339 coupled and moderately coupled with high Δq_l categories. Also, the strong and moderate coupling with high Δθ_l

Deleted: +

Deleted: 4

Deleted: and Table 3

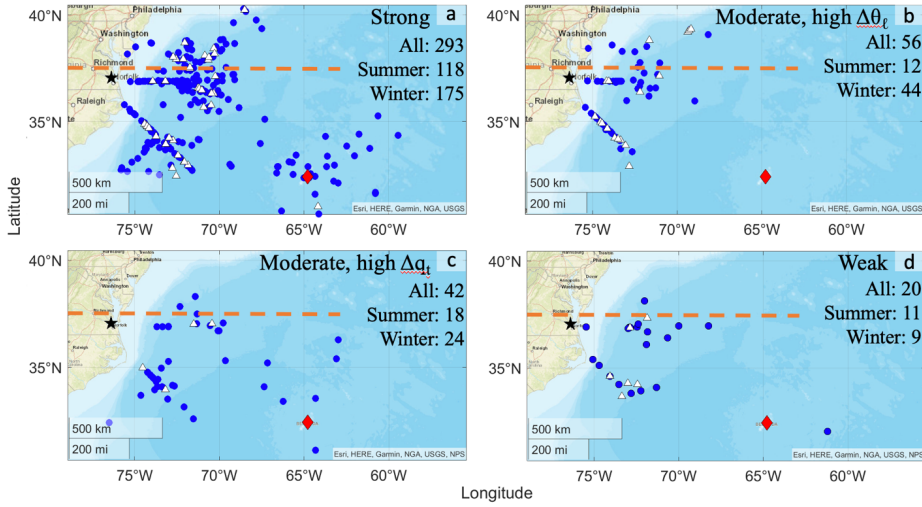
Deleted: .29

Deleted: 3.63

Deleted: .22

Deleted: 4.86

347 categories had more pairs north of 37.5°N (indicated by the orange dashed line), which coincides with more wintertime
 348 sampling of cold air outbreak events that feature turbulent conditions (e.g., Painemal et al., 2021; Kirschler et al.,
 349 2022).
 350



351
 352 **Figure 3: Locations of the BCB segments of the MinAlt-BCB pairs (blue circles), broken up into the four different degrees**
 353 **of coupling. The MinAlt legs were close in time to the BCB legs, so only one spatial map is needed to show the approximate**
 354 **data point location for each pair. The locations of the cloud water samples (white triangles) are overlaid on the BCB segment**
 355 **locations. The black star indicates the location of NASA Langley Research Center, the red diamond indicates Bermuda, and**
 356 **the orange dashed line indicates 37.5°N, which is referenced in the discussion about this figure. The total number of MinAlt-**
 357 **BCB pairs for each category are also included for each coupling regime. The winter months include January, February,**
 358 **March, and April, while the summer months include May, June, August, and September.**
 360

Deleted: ¶

Deleted: ¶

Deleted: ¶

Deleted: ¶

Deleted: ... [1]

Deleted: : (a) strong, (b) moderate, high $\Delta\theta_\ell$, (c) moderate, high Δq_ℓ , and (d) weak

Deleted: and

Deleted: .

Moved (insertion) [1]

Deleted: ¶

Moved up [1]: The winter months include January, February, March, and April, while the summer months include May, June, August, and September.

Deleted: Table 3: Total count of MinAlt-BCB pairs categorized into four coupling categories. The winter months include January, February, March, and April, while the summer months include May, June, August, and September. ¶

... [2]

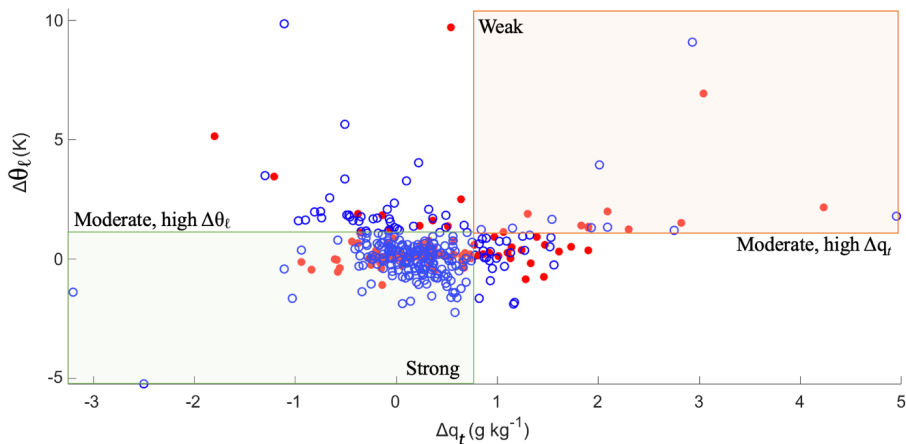
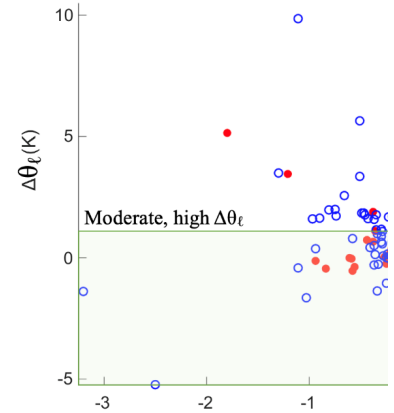


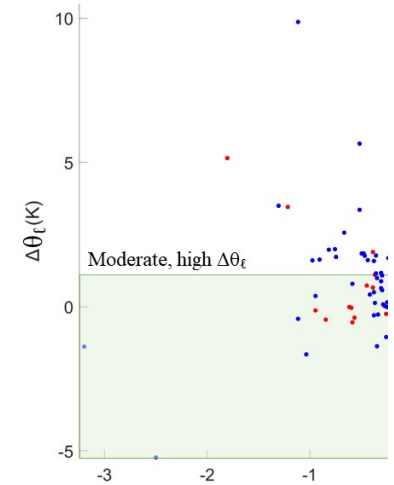
Figure 4; Scatterplot of $\Delta\theta_{\ell}$ vs. Δq_{ℓ} values for the BCB and MinAlt pairs divided into the four coupling regimes, where winter pairs are indicated by blue points and summer pairs are indicated by red points. Refer to Fig. 3 for the number of points in each coupling regime categorized by season. Figure S1 shows this information in the form of a joint frequency histogram.

Figures 3-4 show that there were more MinAlt-BCB pairs during the winter versus summer (252 vs. 159) largely due to the greater ease of sampling such cases with the higher wintertime cloud fraction in the region (Painemal et al., 2021; Kirschler et al., 2022, 2023). But generally, the distribution of coupling categories was the same (summer/winter): 74/70% strongly coupled, 8/18% moderately coupled with high $\Delta\theta_{\ell}$, 11/10% moderately coupled with high Δq_{ℓ} , and 7/4% weakly coupled. The frequency of the moderately coupled with high Δq_{ℓ} category was relatively higher in summer versus winter compared to the other moderate category, which is coincident with the summer having higher temperatures (i.e., higher q_{ℓ}) and more flights farther south in Fig. 3 where temperatures are warmer as compared to farther north.

For context, applying the criteria from past work in Table 1 (Jones et al., 2011; Dong et al., 2015) to this dataset (i.e., Δq_{ℓ} [g kg⁻¹] and $\Delta\theta_{\ell}$ [K] < 0.5 for coupled and all others decoupled) would have led to 206 and 205 coupled and decoupled cases, respectively, with a seasonal breakdown as follows (summer/winter): 43/58% coupled, 35/66% decoupled. However, we caution that the compared vertical levels differ between these studies. For example, Jones et al. (2011) compared levels encompassing more of the full extent of the cloudy MBL (e.g., somewhat analogous to the use of MinAlt and BCT in Fig. 1), whereas in this study we compare MinAlt to BCB due to our focus on aerosol characteristics, which are difficult to measure in clouds. While ACTIVATE flights were designed for achieving a statistically rich dataset portraying the region in an unbiased way, the frequency of occurrence of the four coupling regimes in this study can possibly still be affected by how flights were designed to fly towards areas with relatively



Deleted:



Deleted:

Formatted

[... [3]

Deleted: ure

Formatted: Font: 9 pt, Bold

Deleted: S1 shows the seasonal distribution of the MinAlt-BCB pairs from summer and winter deployments (counts provided in Table Fig. 3). There

Deleted: .21...69.44...0% strongly coupled, 7.55.../17.47...% moderately coupled with high $\Delta\theta_{\ell}$, 11.32.../9.52...0% moderately coupled with high Δq_{ℓ} , and 6.92.../3.57...

[... [4]

Deleted: Δq_{ℓ}

Deleted: $\Delta\theta_{\ell}$

Formatted: Not Superscript/ Subscript

Formatted

[... [5]

Deleted: 2.72...57.2...% coupled, 354.63...665.37

[... [6]

Deleted: Also, ...he frequency of occurrence of the four coupling regimes in this study are driven in part by how

[... [7]

440 higher cloud fraction without complicating scenes such as with multiple cloud layers. We also note that sensitivity
 441 tests were conducted (Table S1) to see how the assignment of MinAlt-BCB pairs to the four coupling categories
 442 changed when accounting for measurement uncertainties, which could push points across the border of their regime
 443 in Fig. 4. Results are preserved with only slight changes in assignments after varying the criteria for Δq_t and $\Delta \theta_t$ by
 444 absolute values of 0.02 in both directions; the same applies using the Jones et al. (2011) criteria, which is shown on
 445 the far right of Table S1. Subsequent effects on other results presented in the following sections were minimal with
 446 the same general conclusions reached.

448 3.2 Aerosol and Atmospheric Properties

449 The results of the aerosol and atmospheric parameter calculations across the four different coupling regimes are
 450 provided in Table 3 (seasonal results in Tables S2-S3), with notched box plots summarizing information from Table 3
 451 in Fig. S2. Of the 411 MinAlt-BCB pairs, 293 were used in aerosol calculations after eliminating pairs that may have
 452 been influenced by rain, cloud, or ice interference. As a note, when quantifying altitudinal differences in variables
 453 across different coupling regimes, the mean at each altitude is used as the comparison parameter unless otherwise
 454 stated, as outliers were already removed prior to data analysis.

456 The first hypothesis of this study is that strongly coupled regimes would have greater turbulence (σ_w) than weakly
 457 coupled regimes. This hypothesis is confirmed when examining σ_w results at both MinAlt (strong/weak = 0.86/0.55
 458 m s⁻¹) and BCB levels (strong/weak = 0.70/0.49 m s⁻¹). The two categories of moderate coupling had greater turbulence
 459 at both altitudes compared to weak coupling, and sometimes had greater turbulence than pairs categorized as strongly
 460 coupled. Further, while BCB σ_w and BCB - MinAlt σ_w had no significant differences across medians, there were some
 461 significant differences across coupling regimes for MinAlt σ_w (Fig. S2). Data in the moderate, high $\Delta \theta_t$ coupling
 462 regime were significantly different from the other regimes, and data categorized as moderate coupling with high Δq_t
 463 were also statistically distinct from the weak coupling regime. This suggests considering multiple coupling regimes
 464 for the northwest Atlantic is important to tease out such nuances as differences in the thermodynamic profiles can
 465 potentially coincide with different aerosol and cloud characteristics as discussed subsequently.

467 **Table 3: Statistics for various atmospheric properties investigated across the MinAlt-BCB pairs (Δ calculation refers to the**
 468 **MinAlt value minus the BCB value), except for MinAlt σ_w and BCB σ_w , which are the average σ_w for each respective leg**
 469 **and for N_a , which is calculated in ACB legs. Each property is broken down into the different degrees of coupling (n = number**
 470 **of points used in each coupling category). Variable acronyms defined in Sect. 2.5. Refer to Fig. S2 for corresponding notched**
 471 **box plots.**

	Degree of Coupling	Mean	Std. Dev.	Min	25%	50%	75%	Max	n
Δ_{scat}	Strong	2.2	2.1	0.00	0.78	1.7	2.8	13.9	274
	Moderate, high $\Delta \theta_t$	3.5	3.5	0.07	0.97	2.4	4.6	14.6	52
	Moderate, high Δq_t	2.4	2.1	0.01	0.70	1.8	3.6	9.2	39
	Weak	3.5	3.3	0.01	0.88	2.2	6.6	10.8	20
Δ_{IntV}	Strong	2.5	2.6	0.02	0.67	1.7	3.5	13.6	288

Deleted: ; thus, the results in Table Fig. 3 and Figure Fig. 4 for instance are not a fully accurate depiction of the actual frequency of occurrence over the northwest Atlantic but rather more of a summary of what was experienced during ACTIVATE flights...

Deleted: Δq_t

Deleted: $\Delta \theta_t$

Formatted: Not Superscript/ Subscript

Formatted: Not Superscript/ Subscript

Deleted: 4

Deleted: 1

Deleted: 2

Deleted: and

Deleted: Table S3 provides sensitivity test results from varying $\Delta \theta_t$ and Δq_t .

Deleted: as

Deleted: as

Deleted: 4

	Moderate, high $\Delta\theta_\ell$	2.1	2.2	0.00	0.46	1.5	2.9	9.3	54
	Moderate, high Δq_f	1.9	1.9	0.01	0.46	1.2	2.8	8.3	41
	Weak	2.8	2.3	0.18	1.0	2.4	4.2	7.6	20
$\Delta N_{a>3\mu m}$	Strong	0.32	0.55	0.00	0.05	0.13	0.35	4.9	288
	Moderate, high $\Delta\theta_\ell$	0.33	0.64	0.00	0.03	0.13	0.31	3.6	54
	Moderate, high Δq_f	0.15	0.14	0.00	0.06	0.11	0.21	0.61	41
	Weak	0.53	1.5	0.01	0.02	0.08	0.27	5.9	20
N_d	Strong	344	217	19	193	310	473	954	238
	Moderate, high $\Delta\theta_\ell$	419	242	45	228	374	610	962	48
	Moderate, high Δq_f	329	154	25	235	327	430	671	31
	Weak	275	181	50	107	245	411	606	18
MinAlt σ_w	Strong	0.86	0.49	0.00	0.47	0.79	1.2	2.4	293
	Moderate, high $\Delta\theta_\ell$	1.0	0.57	0.00	0.52	1.1	1.3	2.2	56
	Moderate, high Δq_f	0.81	0.44	0.00	0.51	0.73	0.99	1.9	42
	Weak	0.55	0.38	0.00	0.19	0.51	0.90	1.3	20
BCB σ_w	Strong	0.70	0.62	0.00	0.26	0.60	1.0	4.0	293
	Moderate, high $\Delta\theta_\ell$	0.64	0.62	0.00	0.00	0.53	1.1	2.2	56
	Moderate, high Δq_f	0.81	0.76	0.00	0.26	0.71	1.1	3.3	42
	Weak	0.49	0.50	0.00	0.04	0.30	0.87	1.6	20
BCB - MinAlt σ_w	Strong	-0.15	0.66	-2.0	-0.45	-0.16	0.10	3.6	285
	Moderate, high $\Delta\theta_\ell$	-0.34	0.57	-2.2	-0.81	-0.23	0.10	0.59	53
	Moderate, high Δq_f	0.01	0.74	-1.6	-0.28	-0.08	0.20	2.9	42
	Weak	-0.05	0.47	-1.1	-0.35	0.01	0.25	0.90	20

488

489 The second hypothesis is that aerosol scattering (Δscat), integrated volume concentration ($0.1 < D_p < 5 \mu\text{m}$; ΔIntV),
490 and giant particle number concentration ($3 < D_p < 50 \mu\text{m}$; $\Delta N_{>3\mu\text{m}}$) would have more vertically homogenous
491 concentrations (i.e., smaller MinAlt-BCB differences) in strongly coupled regimes compared to weakly coupled
492 regimes due to greater mixing for the former as supported by the higher σ_w results already shown. This hypothesis is
493 supported (Table 3 and Fig. S2) since strong coupling cases exhibited lower mean differences (MinAlt-BCB) than
494 weak coupling (Δscat : 2.2/3.5 Mm^{-1} , ΔIntV : 2.5/2.8 $\mu\text{m}^3 \text{cm}^{-3}$, and $\Delta N_{>3\mu\text{m}}$: 0.3/0.5 cm^{-3} , for strong/weak regimes).
495 The third hypothesis was that cloud drop number concentration ($3 < D_p < 50 \mu\text{m}$; N_d) would be greater in strong
496 coupling conditions, as stronger updrafts and turbulence would help to activate more particles into cloud droplets (this
497 was also found in Dong et al., 2015). This is confirmed in Table 3; mean N_d : 344/275 cm^{-3} for strong/weak regimes for
498 ACB legs coinciding with each MinAlt-BCB pair. This result is consistent with past studies for the northwest Atlantic
499 linking stronger turbulence to greater droplet activation efficiency (Kirschler et al., 2022; Dadashazar et al., 2021).
500 The results based on medians agree with those of mean values in Table 3, although medians across regimes for each
501 atmospheric property were not statistically different from one another (Fig. S2).

502

503 When comparing the moderate coupling regimes with the strong and weak regimes, neither Δscat , ΔIntV , nor $\Delta N_{>3\mu\text{m}}$
504 showed a consistent trend in terms of being higher or lower across all three variables. However, one consistent feature
505 among the moderate regimes is that the moderate high Δq_f category showed smaller Δ values than moderate high $\Delta\theta_\ell$
506 for the three aerosol variables. Sometimes, the lowest Δ values did not occur during the strong coupling cases, but
507 rather during moderate coupling with high Δq_f cases (i.e., $\Delta\text{IntV} = 1.9 \mu\text{m}^3 \text{cm}^{-3}$, $\Delta N_{>3\mu\text{m}} = 0.2 \text{cm}^{-3}$). These low
508 differences presumably should coincide with the highest values of σ_w . This is somewhat supported by how BCB σ_w

Deleted: 4

Deleted: 4

Deleted: 4

Deleted: .

Deleted: differences

Deleted: difference calculations with the

515 was greatest for the moderate coupling with high Δq_t regime ($0.81 \pm 0.76 \text{ m s}^{-1}$), although MinAlt σ_w was greatest for
 516 the moderate coupling with high $\Delta\theta_t$ regime ($1.00 \pm 0.57 \text{ m s}^{-1}$) with the value for the moderate coupling with high
 517 Δq_t regime being $0.81 \pm 0.44 \text{ m s}^{-1}$. Also, Appendix A provides discussion in support of why the high Δq_t category
 518 may have small aerosol differences between MinAlt and BCB levels, whereby surface effects may be at play to help
 519 promote mixing in the MBL. Interestingly, the highest N_d values were for the moderate high $\Delta\theta_t$ category with a mean
 520 of 419 cm^{-3} , which can partly be explained by how most of these cases occurred during the winter flights when N_d is
 521 higher than in the summer (see also Tables S2-S3) due to strong updraft velocities that efficiently activate particles
 522 into droplets (e.g., Kirschler et al., 2022). These conditions in winter were common during cold air outbreaks
 523 (Dadashazar et al., 2021).

524

525 3.3 Cloud Water Species

526 67 cloud water samples were used in this study (Table 4), with 60% of the samples falling into the strong coupling
 527 regime, followed by moderate coupling with high $\Delta\theta_t$ (25%), weak coupling (9%), and lastly moderate coupling with
 528 high Δq_t (6%). Locations of samples are shown in Fig. 3. Within the strong coupling and moderate coupling with high
 529 $\Delta\theta_t$ categories, there were several samples north of 37.5°N (marked by orange line in Fig. 3), whereas the moderate
 530 coupling with high Δq_t and weak coupling samples were all south of that latitude. The former two categories include
 531 substantially more data during the winter when air masses typically come from the continent featuring urban emissions
 532 (Dadashazar et al., 2022a).

533

534 **Table 4: Average cloud water mass concentrations ($\mu\text{g m}^{-3}$) and mass fractions (in %, rounded to nearest whole number)**
 535 **for all cloud water samples. Also shown are the pH and $\text{Cl}:\text{Na}^+$ mass ratios. Results are categorized into different degrees**
 536 **of coupling, and the ratio of weak-to-strong coupling is also reported.**

537

	Strong	Moderate, high $\Delta\theta_t$	Moderate, high Δq_t	Weak	Weak : Strong
Mass concentration ($\mu\text{g m}^{-3}$)					
Total	87.45	57.93	91.92	10.32	0.12
Cl^-	45.6	32.0	52.2	4.1	0.09
Na^+	27.9	18.6	29.9	2.5	0.09
Mg^{2+}	3.33	2.22	3.59	0.35	0.10
K^+	0.56	0.37	0.59	0.05	0.09
nss- Ca^{2+}	0.53	0.18	0.17	0.03	0.06
nss- SO_4^{2-}	2.6	1.5	1.7	1.2	0.47
NO_3^-	6.0	2.7	3.3	1.5	0.26
Oxalate	0.10	0.01	0.03	0.01	0.14
NH_4^+	0.89	0.37	0.33	0.56	0.63
Mass fraction (%)					

Deleted: 1

Deleted: and

Deleted: 2

Deleted: 5

Deleted: 59.70

Formatted: Font: Not Italic

Deleted: .37

Deleted: 8.96

Deleted: 5.97

Deleted: 5

Deleted: is

Formatted: Font: Not Bold

Cl ⁻	52	55	57	40	↓
Na ⁺	32	32	33	24	↓
Mg ²⁺	4	4	4	3	↓
K ⁺	↓	↓	↓	↓	↓
nss-Ca ²⁺	↓	0	0	0	↓
nss-SO ₄ ²⁻	3	3	2	12	↓
NO ₃ ⁻	7	5	4	15	↓
Oxalate	0	0	0	0	↓
NH ₄ ⁺	1	↓	0	5	↓
Cl ⁻ :Na ⁺ mass ratio and pH					
pH	4.92	4.60	5.29	4.44	0.90
Cl ⁻ :Na ⁺	1.65	1.66	1.69	1.53	0.92
n	40	17	4	6	

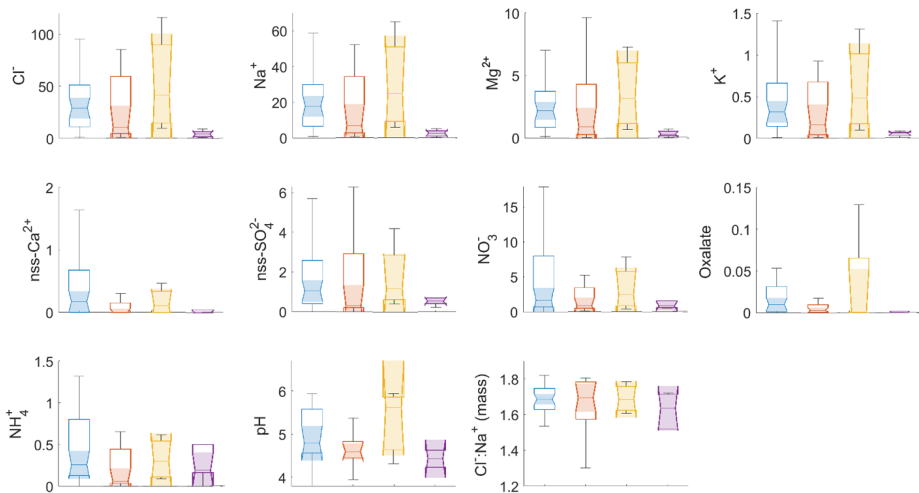
548

549 Figure 5 provides composition statistics for the cloud water samples categorized into the four coupling regimes. As a
 550 note, the notches (and shading) of the box plots help to compare air-equivalent mass concentration medians across the
 551 different coupling categories and aid in the determination of statistical significance. Since this study has utilized means
 552 instead of medians when comparing values across coupling regimes, mean concentrations are provided in the SI
 553 (Tables S4-S6) and the results of Welch's t-tests for each category are given in Table S7. This study also investigated
 554 cumulative average mass concentrations and mass fractions (Table 4) to paint a clearer picture of the breakdown of
 555 chemical species for different degrees of coupling. Based on previous work for stratocumulus clouds over the northeast
 556 Pacific (Wang et al., 2016), we hypothesize that samples from strong coupling regimes would have higher mass
 557 concentrations compared to weakly coupled regimes owing to higher concentrations of sea salt constituents (e.g., Cl⁻,
 558 Na⁺, Mg²⁺, and K⁺). More turbulent conditions in strongly coupled cases are thought to promote more mixing of sea
 559 salt into boundary layer clouds, which can be detected with cloud water composition measurements (e.g., Dadashazar
 560 et al., 2017).

561

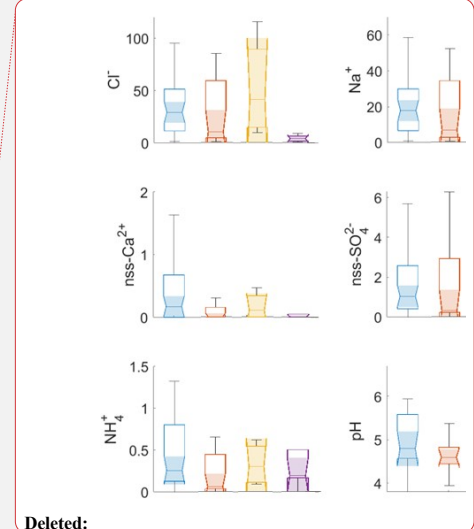
562

Deleted: .11
Deleted: .21
Deleted: 6.79
Deleted: 39.48
Deleted: 0.76
Deleted: 1.94
Deleted: .07
Deleted: 2.56
Deleted: .31
Deleted: 0.76
Deleted: 3.81
Deleted: 3.84
Deleted: 3.91
Deleted: .38
Deleted: 0.89
Deleted: 0.64
Deleted: 0.63
Deleted: 0.65
Deleted: 0.48
Deleted: 0.75
Deleted: 0.60
Deleted: .32
Deleted: .19
Deleted: .31
Deleted: 0.51
Deleted: 2.93
Deleted: 2.65
Deleted: 1.90
Deleted: 1.56
Deleted: 3.95
Deleted: 6.86
Deleted: 4.63
Deleted: 3.63
Deleted: 4.95
Deleted: .18
Deleted: 0.11
Deleted: .01
Deleted: 0.04
Deleted: .13
Deleted: .20
Deleted: .02
Deleted: 0.63
Deleted: 0.35
Deleted: .41
Deleted: .32
Deleted: S3...4-S5...6) and the results of Welch's t-test [8]
Deleted: 5



661
 662 **Figure 5: Notched box plots of species concentrations ($\mu\text{g m}^{-3}$), $\text{Cl}^-:\text{Na}^+$ mass ratio, and pH from cloud water samples**
 663 **collected during periods coinciding with MinAlt-BCB pairs. The box plots are colored according to degree of coupling: blue**
 664 **(strong), red (moderate, high $\Delta\theta$), yellow (moderate, high Δq), and purple (weak). The notches of the boxes assist in the**
 665 **determination of statistical significance between multiple medians (the shading indicates where the notches begin and end).**
 666 **If notches/shading do not overlap, the medians are statistically different from one another (also referred to as statistically**
 667 **significant). Table S7 provides the results of Welch's t-tests, which compares the means of two groups and determines if**
 668 **they are statistically different. The tests were performed on the mean cloud water concentrations of these nine chemical**
 669 **species, pH, and $\text{Cl}^-:\text{Na}^+$.**

670
 671 Strong coupling regime samples exhibit higher average mass concentrations compared to weak coupling, and Na^+ , Cl^- ,
 672 K^+ , and NO_3^- were all found to be statistically different across the two regimes (p-values: 1.07E^{-4} , 3.54E^{-5} , 5.52E^{-5} ,
 673 and 9.57E^{-3} , respectively). The most abundant species by mass across the coupling regimes were usually Cl^- , Na^+ , and
 674 NO_3^- , similar to the results of Wang et al. (2016). Further, although lower in absolute mass concentration, some species
 675 were relatively more abundant (i.e., higher mass fraction) in the weak coupling regime: nss-SO_4^{2-} (12% [weak] vs. 3%
 676 [strong]), NO_3^- (15% [weak] vs. 7% [strong]), NH_4^+ (5% [weak] vs. 1% [strong]). Oxalate was very low in overall
 677 concentration and exhibited comparable mass fractions. These results are consistent with the idea of surface emissions
 678 (mainly sea salt) driving cloud water composition in turbulent conditions (i.e., strongly coupled) in contrast to weakly
 679 coupled clouds that have much lower overall mass concentrations of the reported ions but relatively more influence
 680 from non-sea salt species. The two moderate coupling regimes include samples with concentration and mass fraction
 681 values more similar to the strongly coupled regime, with even higher sea salt tracer species concentrations for the
 682 moderate high Δq regime. This is consistent with the aerosol results in Sect. 3.2 that suggest this latter category can
 683 have appreciable influence from the surface, although it is also important to note that this is based on 4 cloud water
 684 samples.



Deleted:

Deleted: S6
 Deleted: 1

Deleted: 1.56%
 Deleted: 2.9
 Deleted: 4.95
 Deleted: 6.86
 Deleted: .41
 Deleted: .02
 Deleted: : 0.13% [weak] vs. 0.11% [strong]
 Deleted: ed

696
697 Wang et al. (2016) analyzed 35 cloud water constituents for northeast Pacific stratocumulus clouds and found that 27
698 chemical species were higher in coupled clouds, with the remaining eight (acetate, formate, Si, NO₂⁻, Al, Mn, Cr, and
699 Co) higher in decoupled clouds due to relatively more continental influence. The 27 cloud water species that were
700 higher in coupled clouds were associated with a mix of anthropogenic and natural sources (i.e., sea salt emissions for
701 Cl⁻ and Na⁺). Conversely, the eight species that were higher in decoupled clouds were associated with crustal matter
702 and biogenic sources. Several of the most abundant species from our study (Na⁺, Cl⁻, Mg²⁺) are common sea salt
703 tracers, while NO₃⁻ sources in the region may include ocean sea spray and biogenic emissions, wildfires, agricultural
704 emissions, and ship exhaust (Corral et al., 2020; Corral et al., 2021; Corral et al., 2022; Shah et al., 2018). Note that
705 nitric acid can partition effectively into cloud droplets as well, which can drive up cloud water NO₃⁻ levels (e.g.,
706 Prabhakar et al., 2014). At least some of the species with higher mass fractions in the weakly coupled regime (e.g.,
707 nss-SO₄²⁻, NO₃⁻) have previously been linked to combustion sources in this region, such as industrial emissions and
708 transportation (Brock et al., 2008; Song et al., 2001). Ammonium is a major base forming salts with nss-SO₄²⁻ and
709 NO₃⁻, whereas oxalate has diverse sources (e.g., continental, marine) and can be associated with sea salt and produced
710 via cloud processing (e.g., Stahl et al., 2020; Hilario et al., 2021). Nss-Ca²⁺ is often associated with continental crustal
711 matter (Ma et al., 2021; Edwards et al., 2024), and its concentrations are generally very low, suggestive of low influence
712 from dust during the majority of ACTIVATE flights.

713
714 In addition to examining mass concentrations, we also examined pH and the Cl⁻:Na⁺ ratio. Regarding the latter ratio, sea
715 salt chloride concentrations can be reduced in the presence of acidic species such as sulfuric and nitric acids (e.g.,
716 Braun et al., 2017; Edwards et al., 2024). This phenomenon is known as Cl⁻ depletion, and it can be calculated by
717 taking the ratio of Cl⁻:Na⁺. For context, Wang et al. (2016) reported no major difference in the Cl⁻:Na⁺ ratio in cloud
718 water over the northeast Pacific but measured lower pH in coupled clouds (4.26) versus decoupled clouds (4.48). In
719 this study, samples in the weak coupling regime exhibited the lowest pH (4.4 vs. 5.0 for strong coupling) and Cl⁻:Na⁺
720 (1.5 vs. 1.7 for strong coupling), which potentially could be related to the higher relative amount of nss-SO₄²⁻, NO₃⁻.
721 The two moderate coupling regimes feature samples with pH and Cl⁻:Na⁺ values more similar to strongly coupled
722 samples.

723
724 A limitation in this analysis is that there were only six cloud water samples that fell into the weak coupling regime.
725 Future work examining the sensitivity of aerosol and cloud characteristics to coupling regimes should try to obtain
726 better sampling coverage across all regimes.

727 728 **4 Conclusions**

729 This study used data collected during the NASA ACTIVATE mission (2020–2022) from the HU-25 Falcon to assess
730 the frequency of different degrees of MBL cloud coupling and also how aerosol and cloud characteristics varied among
731 four such regimes. MinAlt and BCB legs were used to assess thermodynamic statistics along with turbulence, aerosol,
732 and cloud variables, which were calculated at each leg and the differences of the two legs were taken for final

Deleted: . Similar to oxalate, these

Deleted: a

Deleted: of

736 comparison metrics. Cloud water species and N_d values associated with MinAlt and BCB pairs were analyzed when
737 cloud sampling occurred within 30 minutes of a MinAlt-BCB pair.

738
739 Vertical profiles between MinAlt and BCB pairs were divided into four degrees of coupling: strongly coupled ($\Delta q_t \leq$
740 0.8 g kg^{-1} , $\Delta\theta_t \leq 1.0 \text{ K}$), moderately coupled with high $\Delta\theta_t$ ($\Delta q_t \leq 0.8 \text{ g kg}^{-1}$, $\Delta\theta_t > 1.0 \text{ K}$), moderately coupled with
741 high Δq_t ($\Delta q_t > 0.8 \text{ g kg}^{-1}$, $\Delta\theta_t \leq 1.0 \text{ K}$), and weakly coupled ($\Delta q_t > 0.8 \text{ g kg}^{-1}$, $\Delta\theta_t > 1.0 \text{ K}$). In total, 411 MinAlt-BCB
742 pairs were investigated, along with 67 cloud water samples. Using this coupling categorization criteria, only a handful
743 of weakly coupled MBL clouds were detected (20, compared to 286 with strong coupling). The relative amounts of
744 the regimes did not vary substantially between the winter and summer seasons. Instead, particular focus was placed
745 on comparing regimes with strong coupling to those with weak coupling. Support for the coupling criteria was sought
746 through five different aerosol/cloud/dynamic parameters (Δscat , ΔIntV , $\Delta N_{>3\mu\text{m}}$, N_d , and σ_w) and 11 cloud water
747 variables (nss- Ca^{2+} , Cl^- , K^+ , Mg^{2+} , Na^+ , NH_4^+ , NO_3^- , oxalate, nss- SO_4^{2-} , pH, $\text{Cl}:\text{Na}^+$). Turbulence was generally greater
748 during regimes of strong coupling compared to weak coupling, which corresponded to lower values of Δscat , ΔIntV ,
749 and $\Delta N_{>3\mu\text{m}}$ due to better presumed mixing in the MBL. N_d was higher for strong coupling regimes, as higher
750 turbulence likely encouraged more cloud drop activation, which was also observed in Dong et al. (2015) for the
751 northeast Atlantic. Sea salt tracers (e.g., Na^+ , Cl^- , and K^+) were higher in concentration in strongly coupled compared
752 to weakly coupled MBL clouds and were found to have statistically significant differences across the two coupling
753 regimes. Additionally, nss- SO_4^{2-} , NO_3^- , and NH_4^+ , which are linked to continental sources, were found in higher mass
754 fractions during weak coupling regimes; this was also observed in Wang et al. (2016) for northeast Pacific
755 stratocumulus clouds, corresponding to lower values of both cloud water pH and the $\text{Cl}:\text{Na}^+$ ratio.

756
757 The inclusion of two moderate coupling categories is shown to be insightful as differences between the two potentially
758 can be explained by the relative influence of subsidence/entrainment versus surface effects. More specifically, the
759 moderately coupled category with high $\Delta\theta_t$ is thought to be influenced more by processes above the MBL such as
760 entrainment of dry air with high potential temperature whereas the other moderate category with high Δq_t likely has
761 more influence from surface processes. These speculations are supported by how the moderate high Δq_t regime
762 exhibited even more turbulent mixing than the strong coupling regime, yielding the highest sea salt concentrations in
763 cloud water and the lowest values of ΔIntV and $\Delta N_{>3\mu\text{m}}$. Furthermore, the moderate high $\Delta\theta_t$ category exhibited the
764 highest mean N_d value (419 cm^{-3}) of any category ($275\text{-}344 \text{ cm}^{-3}$ for the other three categories), which can be explained
765 partly by how most of these cases (44 of 56) were in winter flights when N_d is typically higher than summer, especially
766 during cold air outbreaks (e.g., Dadashazar et al., 2021).

767
768 This study is the first to our knowledge to investigate degrees of coupling in MBL clouds through thermodynamic
769 statistics in the northwest Atlantic with a focus on aerosol and cloud microphysical characteristics. Further research
770 of this nature is needed in other regions to assess thermodynamic criteria for MBL cloud to surface coupling, including
771 how aerosol and cloud characteristics change with degrees of MBL coupling in different regions. The results here
772 indicate that a failure to account for different coupling regimes can mix together varying aerosol and cloud

Deleted: +

Deleted:

Deleted: , which

776 microphysical characteristics in data analysis studies, which increases risk of separating out important details such as
777 how cloud composition is very different across the spectrum of cloud coupling strength. A limitation of this study to
778 build on is obtaining more statistics for the more weakly coupled category, which in part may be influenced by how
779 flight plans are designed. The results of this research have important implications for studies of aerosol-cloud
780 interactions, as not considering coupling strength will make interpretations difficult, as we have shown important
781 differences for aerosol and cloud properties.

782

783 **Appendix A. Discussion of the two moderate regimes**

784 To help with the interpretation of the two moderate regimes defined in Table 1, we provide a perspective based on the
785 following discussion. Using equation 1 but expanding it to take the difference of the liquid water potential temperature
786 between the BCB and MinAlt flight legs yields the following:

$$787 \Delta\theta_\ell = (\theta_{BCB} - \left(\frac{L_v}{c_{pd}}\right) \times q_{\ell,BCB}) - (\theta_{MinAlt} - \left(\frac{L_v}{c_{pd}}\right) \times q_{\ell,MinAlt}) \quad (A1)$$

788 Note that both q_ℓ terms are small below cloud. The $\Delta\theta_\ell$ value can thus be large due to large-scale subsidence or
789 entrainment when dry air from free troposphere with high θ which is potentially mixed with air at the BCB level.
790 While θ_{MinAlt} can be high due to surface heating, it acts to reduce $\Delta\theta_\ell$. Also, the current MinAlt is slightly above the
791 typical surface layer and hence the surface inversion. Also, note that:

$$792 \Delta q_t = (q_{v,MinAlt} + q_{l,MinAlt}) - (q_{v,BCB} + q_{l,BCB}) \quad (A2)$$

793 where both q_t terms are small below cloud and are typically much smaller than q_v . The range of q_v is largely controlled
794 by the temperature due to the Clapeyron-Clausius equation (the higher temperature, the higher saturation vapor
795 pressure). While high Δq_t may be due to low q_v at the BCB level, it is more likely due to high q_v near the surface
796 because saturation vapor pressure exponentially increases with temperature.

797 To conclude, the $\Delta\theta_\ell$ term is more likely influenced by features above the MBL while the Δq_t term is more likely
798 influenced by near-surface effects.

799

800 **Data availability**

801 The ACTIVATE dataset can be downloaded at <https://doi.org/10.5067/SUBORBITAL/ACTIVATE/DATA001>
802 (ACTIVATE Science Team, 2020).

803

804 **Author contributions**

805 YC, EC, JPD, GSD, MAF, SK, JBN, MAS, KLT, CV, ELW, and LDZ collected and/or prepared the data. KTZ, SD,
806 and KM conducted data analysis. KTZ, KM, and SD conducted the formal investigation. KTZ, LWS, and AS
807 conducted data interpretation. KTZ and AS prepared the manuscript with editing from all co-authors.

808

809 **Competing interests**

810 At least one of the (co-)authors is a member of the editorial board of Atmospheric Chemistry and Physics.

811

812 **Disclaimer**

813 Publisher's note: Copernicus Publications remains neutral with regard to jurisdictional claims in published maps and
814 institutional affiliations.

815

816 **Acknowledgements**

817 We thank the pilots and aircraft maintenance personnel of NASA Langley Research Services Directorate for
818 conducting ACTIVATE flights and all others who were involved in executing the ACTIVATE campaign.

819

820 **Financial support**

821 ACTIVATE is a NASA Earth Venture Suborbital-3 (EVS-3) investigation funded by NASA's Earth Science Division
822 and managed through the Earth System Science Pathfinder Program Office. University of Arizona investigators were
823 supported by NASA grant no. 80NSSC19K0442 and ONR grant no. N00014-21-1-2115. CV and SK were funded by
824 DFG SPP-1294 HALO under project no. 522359172 and by the European Union's Horizon Europe program through
825 the Single European Sky ATM Research 3 Joint Undertaking projects CONCERTO (grant no 101114785) and
826 CICONIA (grant no 101114613).

827 **References**

- 828 ACTIVATE Science Team: Aerosol Cloud meteorology Interactions over the western Atlantic Experiment Data,
829 <https://doi.org/10.5067/SUBORBITAL/ACTIVATE/DATA001>, 2020.
- 830 Andreae, M. O., Elbert, W., Cai, Y., Andreae, T. W., and Gras, J.: Non-sea-salt sulfate, methanesulfonate, and nitrate
831 aerosol concentrations and size distributions at Cape Grim, Tasmania, *Journal of Geophysical Research:*
832 *Atmospheres*, 104, 21695-21706, <https://doi.org/10.1029/1999JD900283>, 1999.
- 833 Ayers, G. P., Ivey, J. P., and Gillett, R. W.: Coherence between seasonal cycles of dimethyl sulphide,
834 methanesulphonate and sulphate in marine air, *Nature*, 349, 404-406, <https://doi.org/10.1038/349404a0>, 1991.
- 835 AzadiAghdam, M., Braun, R. A., Edwards, E.-L., Bañaga, P. A., Cruz, M. T., Betito, G., Cambaliza, M. O.,
836 Dadashazar, H., Lorenzo, G. R., Ma, L., MacDonald, A. B., Nguyen, P., Simpas, J. B., Stahl, C., and Sorooshian,
837 A.: On the nature of sea-salt aerosol at a coastal megacity: Insights from Manila, Philippines in Southeast Asia,
838 *Atmospheric Environment*, 216, 116922, <https://doi.org/10.1016/j.atmosenv.2019.116922>, 2019.
- 839 Bretherton, C. S. and Wyant, M. C.: Moisture transport, lower-tropospheric stability, and decoupling of cloud-topped
840 boundary layers, *Journal of the Atmospheric Sciences*, 54, 148-167, [https://doi.org/10.1175/1520-0469\(1997\)054<0148:MTLTA>2.0.CO;2](https://doi.org/10.1175/1520-0469(1997)054<0148:MTLTA>2.0.CO;2), 1997.
- 842 Bretherton, C. S., Wood, R., George, R. C., Leon, D., Allen, G., and Zheng, X.: Southeast Pacific stratocumulus clouds,
843 precipitation and boundary layer structure sampled along 20° S during VOCALS-REx, *Atmospheric Chemistry*
844 *and Physics*, 10, 10639-10654, <https://doi.org/10.5194/acp-10-10639-2010>, 2010.
- 845 Brock, C.A., Sullivan, A.P., Peltier, R.E., Weber, R.J., Wollny, A., De Gouw, J.A., Middlebrook, A.M., Atlas, E.L.,
846 Stohl, A., Trainer, M.K. and Cooper, O.R.: Sources of particulate matter in the northeastern United States in
847 summer: 2. Evolution of chemical and microphysical properties, *Journal of Geophysical Research:*
848 *Atmospheres*, 113, D8, <https://doi.org/10.1029/2007JD009241>, 2008.
- 849 Brümmer, B.: Boundary layer mass, water, and heat budgets in wintertime cold-air outbreaks from the Arctic sea ice,
850 *Monthly Weather Review*, 125, 1824-1837, [https://doi.org/10.1175/1520-0493\(1997\)125<1824:BLMWAH>2.0.CO;2](https://doi.org/10.1175/1520-0493(1997)125<1824:BLMWAH>2.0.CO;2), 1997.
- 852 Brunke, M. A., Cutler, L., Urzua, R. D., Corral, A. F., Crosbie, E., Hair, J., Hostetler, C., Kirschler, S., Larson, V., Li,
853 X.-Y., Ma, P.-L., Minke, A., Moore, R., Robinson, C. E., Scarino, A. J., Schlosser, J., Shook, M., Sorooshian, A.,
854 Thornhill, K. L., Voigt, C., Wan, H., Wang, H., Winstead, E., Zeng, X., Zhang, S., and Ziemba, L. D.: Aircraft
855 observations of turbulence in cloudy and cloud-free boundary layers over the western North Atlantic Ocean from
856 ACTIVATE and implications for the Earth system model evaluation and development, *Journal of Geophysical*
857 *Research: Atmospheres*, 127, e2022JD036480, <https://doi.org/10.1029/2022JD036480>, 2022.
- 858 Corral, A.F., Dadashazar, H., Stahl, C., Edwards, E.-L., Zuidema, P., and Sorooshian, A.: Source apportionment of
859 aerosol at a coastal site and relationships with precipitation chemistry: A case study over the southeast United
860 States, *Atmosphere*, 11, 1212, <https://doi.org/10.3390/atmos11111212>, 2020.
- 861 Corral, A. F., Braun, R. A., Cairns, B., Gorooh, V. A., Liu, H., Ma, L., Mardi, A. H., Painemal, D., Starnes, S., van
862 Dierenhoven, B., Wang, H., Yang, Y., Zhang, B., and Sorooshian, A.: An overview of atmospheric features over
863 the western North Atlantic Ocean and North American east coast – Part 1: Analysis of aerosols, gases, and wet

864 deposition chemistry, *Journal of Geophysical Research: Atmospheres*, 126, e2020JD032592,
865 <https://doi.org/10.1029/2020JD032592>, 2021.

866 Corral, A. F., Choi, Y., Collister, B. L., Crosbie, E., Dadashazar, H., DiGangi, J. P., Diskin, G. S., Fenn, M., Kirschler,
867 S., Moore, R. H., Nowak, J. B., Shook, M. A., Stahl, C. T., Shingler, T., Thornhill, K. L., Voigt, C., Ziemba, L.
868 D., and Sorooshian, A.: Dimethylamine in cloud water: a case study over the northwest Atlantic Ocean,
869 *Environmental Science: Atmospheres*, 2, 1534-1550, <https://doi.org/10.1039/d2ea00117a>, 2022.

870 Crosbie, E., Brown, M. D., Shook, M., Ziemba, L., Moore, R. H., Shingler, T., Winstead, E., Thornhill, K. L.,
871 Robinson, C., MacDonald, A. B., Dadashazar, H., Sorooshian, A., Beyersdorf, A., Eugene, A., Collett Jr, J.,
872 Straub, D., and Anderson, B.: Development and characterization of a high-efficiency, aircraft-based axial cyclone
873 cloud water collector, *Atmospheric Measurement Techniques*, 11, 5025-5048, [https://doi.org/10.5194/amt-11-](https://doi.org/10.5194/amt-11-5025-2018)
874 [5025-2018](https://doi.org/10.5194/amt-11-5025-2018), 2018.

875 Dadashazar, H., Wang, Z., Crosbie, E., Brunke, M., Zeng, X., Jonsson, H., Woods, R. K., Flagan, R. C., Seinfeld, J.
876 H., and Sorooshian, A.: Relationships between giant sea salt particles and clouds inferred from aircraft
877 physicochemical data, *Journal of Geophysical Research Atmospheres*, 122, 3421–3434,
878 <https://doi.org/10.1002/2016JD026019>, 2017.

879 Dadashazar, H., Painemal, D., Alipanah, M., Brunke, M., Chellappan, S., Corral, A. F., Crosbie, E., Kirschler, S., Liu,
880 H., Moore, R. H., Robinson, C., Scarino, A. J., Shook, M., Sinclair, K., Thornhill, K. L., Voigt, C., Wang, H.,
881 Winstead, E., Zeng, X., Ziemba, L., Zuidema, P., and Sorooshian, A.: Cloud drop number concentrations over the
882 western North Atlantic Ocean: seasonal cycle, aerosol interrelationships, and other influential factors,
883 *Atmospheric Chemistry and Physics*, 21, 10499-10526, <https://doi.org/10.5194/acp-21-10499-2021>, 2021.

884 Dadashazar, H., Corral, A. F., Crosbie, E., Dmitrovic, S., Kirschler, S., McCauley, K., Moore, R., Robinson, C.,
885 Schlosser, J. S., Shook, M., Thornhill, K. L., Voigt, C., Winstead, E., Ziemba, L., and Sorooshian, A.: Organic
886 enrichment in droplet residual particles relative to out of cloud over the northwestern Atlantic: analysis of airborne
887 ACTIVATE data, *Atmospheric Chemistry and Physics*, 22, 13897-13913, [https://doi.org/10.5194/acp-22-13897-](https://doi.org/10.5194/acp-22-13897-2022)
888 [2022](https://doi.org/10.5194/acp-22-13897-2022), 2022a

889 Dadashazar, H.; Crosbie, E.; Choi, Y.; Corral, A.F.; DiGangi, J.P.; Diskin, G.S.; Dmitrovic, S.; Kirschler, S.; McCauley,
890 K.; Moore, R.H.; et al.: Analysis of MONARC and ACTIVATE airborne aerosol data for aerosol-cloud interaction
891 investigations: Efficacy of stairstepping flight legs for airborne in situ sampling, *Atmosphere*, 13, 1242,
892 <https://doi.org/10.3390/atmos13081242>, 2022b.

893 Diskin, G., Podolske, J., Sachse, G., and Slate, T.: Open-path airborne tunable diode laser hygrometer. *Society of*
894 *Photo-Optical Instrumentation Engineers*, 4817, <https://doi.org/10.1117/12.453736>, 2002.

895 Dong, X., Schwantes, A. C., Xi, B., and Wu, P.: Investigation of the marine boundary layer cloud and CCN properties
896 under coupled and decoupled conditions over the Azores, *Journal of Geophysical Research: Atmospheres*, 120,
897 6179-6191, <https://doi.org/10.1002/2014JD022939>, 2015.

898 Edwards, E. L., Choi, Y., Crosbie, E. C., DiGangi, J. P., Diskin, G. S., Robinson, C. E., Shook, M. A., Winstead, E. L.,
899 Ziemba, L. D., and Sorooshian, A.: Sea-salt reactivity over the northwest Atlantic: an in-depth look using the

900 airborne ACTIVATE dataset, *Atmospheric Chemistry and Physics*, 24, 3349-3378, 10.5194/acp-24-3349-2024,
901 2024.

902 Froyd, K. D., Murphy, D. M., Brock, C. A., Campuzano-Jost, P., Dibb, J. E., Jimenez, J. L., Kupc, A., Middlebrook,
903 A. M., Schill, G. P., Thornhill, K. L., Williamson, C. J., Wilson, J. C., and Ziemba, L. D.: A new method to
904 quantify mineral dust and other aerosol species from aircraft platforms using single-particle mass spectrometry.
905 *Atmospheric Measurement Techniques*, 12, 11, 6209-6239, <https://doi.org/10.5194/amt-12-6209-2019>, 2019.

906 Gonzalez, M. E., Corral, A. F., Crosbie, E., Dadashazar, H., Diskin, G. S., Edwards, E.-L., Kirschler, S., Moore, R.
907 H., Robinson, C. E., Schlosser, J. S., Shook, M., Stahl, C., Thornhill, K. L., Voigt, C., Winstead, E., Ziemba, L.
908 D., and Sorooshian, A.: Relationships between supermicrometer particle concentrations and cloud water sea-salt
909 and dust concentrations: analysis of MONARC and ACTIVATE data, *Environmental Science: Atmospheres*, 2,
910 738-752, <https://doi.org/10.1039/D2EA00049K>, 2022.

911 Goren, T., Rosenfeld, D., Sourdeval, O., and Quaas, J.: Satellite observations of precipitating marine stratocumulus
912 show greater cloud fraction for decoupled clouds in comparison to coupled clouds, *Geophysical Research Letters*,
913 45, 5126-5134, <https://doi.org/10.1029/2018GL078122>, 2018.

914 Griesche, H. J., Ohneiser, K., Seifert, P., Radenz, M., Engelmann, R., and Ansmann, A.: Contrasting ice formation in
915 Arctic clouds: surface-coupled vs. surface-decoupled clouds, *Atmospheric Chemistry and Physics*, 21, 10357-
916 10374, <https://doi.org/10.5194/acp-21-10357-2021>, 2021.

917 Hilario, M. R. A., Crosbie, E., Bañaga, P. A., Betito, G., Braun, R. A., Cambaliza, M. O., Corral, A. F., Cruz, M. T.,
918 Dibb, J. E., Lorenzo, G. R., MacDonald, A. B., Robinson, C. E., Shook, M. A., Simpas, J. B., Stahl, C., Winstead,
919 E., Ziemba, L. D., and Sorooshian, A.: Particulate oxalate-to-sulfate ratio as an aqueous processing marker:
920 Similarity across field campaigns and limitations, *Geophysical Research Letters*, 48, e2021GL096520,
921 <https://doi.org/10.1029/2021GL096520>, 2021.

922 Jones, C. R., Bretherton, C. S., and Leon, D.: Coupled vs. decoupled boundary layers in VOCALS-REx, *Atmospheric*
923 *Chemistry and Physics*, 11, 7143-7153, <https://doi.org/10.5194/acp-11-7143-2011>, 2011.

924 Kirschler, S., Voigt, C., Anderson, B., Campos Braga, R., Chen, G., Corral, A. F., Crosbie, E., Dadashazar, H., Ferrare,
925 R. A., Hahn, V., Hendricks, J., Kaufmann, S., Moore, R., Pöhlker, M. L., Robinson, C., Scarino, A. J.,
926 Schollmayer, D., Shook, M. A., Thornhill, K. L., Winstead, E., Ziemba, L. D., and Sorooshian, A.: Seasonal
927 updraft speeds change cloud droplet number concentrations in low-level clouds over the western North Atlantic.
928 *Atmospheric Chemistry and Physics*, 22, 12, 8299-8319, <https://doi.org/10.5194/acp-22-8299-2022>, 2022.

929 Kirschler, S., Voigt, C., Anderson, B. E., Chen, G., Crosbie, E. C., Ferrare, R. A., Hahn, V., Hair, J. W., Kaufmann, S.,
930 Moore, R. H., Painemal, D., Robinson, C. E., Sanchez, K. J., Scarino, A. J., Shingler, T. J., Shook, M. A.,
931 Thornhill, K. L., Winstead, E. L., Ziemba, L. D., and Sorooshian, A.: Overview and statistical analysis of
932 boundary layer clouds and precipitation over the western North-Atlantic Ocean. *EGUsphere*, 1-29.
933 <https://doi.org/10.5194/egusphere-2023-898>, 2023.

934 Korhonen, H., Carslaw, K. S., Spracklen, D. V., Mann, G. W., and Woodhouse, M. T.: Influence of oceanic dimethyl
935 sulfide emissions on cloud condensation nuclei concentrations and seasonality over the remote Southern

936 Hemisphere oceans: A global model study, *Journal of Geophysical Research: Atmospheres*, 113,
937 <https://doi.org/10.1029/2007JD009718>, 2008.

938 Ma, L., Dadashazar, H., Hilario, M. R. A., Cambaliza, M. O., Lorenzo, G. R., Simpas, J. B., Nguyen, P., and
939 Sorooshian, A.: Contrasting wet deposition composition between three diverse islands and coastal North
940 American sites, *Atmospheric Environment*, 244, 117919, <https://doi.org/10.1016/j.atmosenv.2020.117919>, 2021.

941 MacDonald, A. B., Hossein Mardi, A., Dadashazar, H., Azadi Aghdam, M., Crosbie, E., Jonsson, H. H., Flagan, R. C.,
942 Seinfeld, J. H., and Sorooshian, A.: On the relationship between cloud water composition and cloud droplet
943 number concentration. *Atmos. Chem. Phys.*, 20, 13, 7645-7665, <https://doi.org/10.5194/acp-20-7645-2020>, 2020.

944 McNaughton, C. S., Clarke, A. D., Howell, S. G., Pinkerton, M., Anderson, B., Thornhill, L., Hudgins, C., Winstead,
945 E., Dibb, J. E., Scheuer, E., and Maring, H.: Results from the DC-8 Inlet Characterization Experiment (DICE):
946 Airborne versus surface sampling of mineral dust and sea-salt aerosols, *Aerosol Science and Technology*, 41, 136-
947 159, <https://doi.org/10.1080/02786820601118406>, 2007.

948 Nicholls, S.: The dynamics of stratocumulus: Aircraft observations and comparisons with a mixed layer model,
949 *Quarterly Journal of the Royal Meteorological Society*, 110, 783-820, <https://doi.org/10.1002/qj.49711046603>,
950 1984.

951 Painemal, D., Corral, A. F., Sorooshian, A., Brunke, M. A., Chellappan, S., Afzali Goroooh, V., Ham, S.-H., O'Neill,
952 L., Smith Jr., W. L., Tselioudis, G., Wang, H., Zeng, X., and Zuidema, P.: An overview of atmospheric features
953 over the western North Atlantic ocean and North American east coast—Part 2: Circulation, boundary layer, and
954 clouds, *Journal of Geophysical Research: Atmospheres*, 126, e2020JD033423,
955 <https://doi.org/10.1029/2020JD033423>, 2021.

956 Painemal, D., Chellappan, S., Smith Jr., W. L., Spangenberg, D., Park, J. M., Ackerman, A., Chen, J., Crosbie, E.,
957 Ferrare, R., Hair, J., Kirschler, S., Li, X.-Y., McComiskey, A., Moore, R. H., Sanchez, K., Sorooshian, A., Tornow,
958 F., Voigt, C., Wang, H., Winstead, E., Zeng, X., Ziemba, L., and Zuidema, P.: Wintertime synoptic patterns of
959 midlatitude boundary layer clouds over the western North Atlantic: Climatology and insights from in situ
960 ACTIVATE observations, *Journal of Geophysical Research: Atmospheres*, 128, e2022JD037725,
961 <https://doi.org/10.1029/2022JD037725>, 2023.

962 Prabhakar, G., Ervens, B., Wang, Z., Maudlin, L. C., Coggon, M. M., Jonsson, H. H., Seinfeld, J. H., and Sorooshian,
963 A.: Sources of nitrate in stratocumulus cloud water: Airborne measurements during the 2011 E-PEACE and 2013
964 NiCE studies, *Atmospheric Environment*, 97, 166-173, <https://doi.org/10.1016/j.atmosenv.2014.08.019>, 2014.

965 Papritz, L. and Spengler, T.: Analysis of the slope of isentropic surfaces and its tendencies over the North Atlantic,
966 *Quarterly Journal of the Royal Meteorological Society*, 141, 3226-3238, <https://doi.org/10.1002/qj.2605>, 2015.

967 Ramanathan, V., Cess, R. D., Harrison, E. F., Minnis, P., Barkstrom, B. R., Ahmad, E., and Hartmann, D. Cloud-
968 radiative forcing and climate: Results from the Earth Radiation Budget Experiment. *Science*, 243, 4887, 57-63,
969 <https://doi.org/doi:10.1126/science.243.4887.57/>, 1989.

970 Seethala, C., Zuidema, P., Edson, J., Brunke, M., Chen, G., Li, X.-Y., Painemal, D., Robinson, C., Shingler, T., Shook,
971 M., Sorooshian, A., Thornhill, L., Tornow, F., Wang, H., Zeng, X., and Ziemba, L.: On assessing ERA5 and

972 MERRA2 representations of cold-air outbreaks across the Gulf Stream, *Geophysical Research Letters*, 48,
973 e2021GL094364, <https://doi.org/10.1029/2021GL094364>, 2021.

974 Shah, V., Jaeglé, L., Thornton, J. A., Lopez-Hilfiker, F. D., Lee, B. H., Schroder, J. C., Campuzano-Jost, P., Jimenez,
975 J. L., Guo, H., Sullivan, A.P., Weber, R. J., Green, J. R., Fiddler, M. N., Bililign, S., Campos, T. L., Stell, M.,
976 Weinheimer, A.J., Montzka, D. D., and Brown, S. S.: Chemical feedbacks weaken the wintertime response of
977 particulate sulfate and nitrate to emissions reductions over the eastern United States, *National Academy of*
978 *Sciences*, 115, 8110-8115, <https://doi.org/10.1073/pnas.1803295115>, 2018.

979 Song, X.H., Polissar, A.V. and Hopke, P.K.: Sources of fine particle composition in the northeastern US, *Atmospheric*
980 *Environment*, 35, 31, 5277-5286, [https://doi.org/10.1016/S1352-2310\(01\)00338-7](https://doi.org/10.1016/S1352-2310(01)00338-7), 2001.

981 Sorooshian, A., Anderson, B., Bauer, S. E., Braun, R. A., Cairns, B., Crosbie, E., Dadashazar, H., Diskin, G., Ferrare,
982 R., Flagan, R. C., Hair, J., Hostetler, C., Jonsson, H. H., Kleb, M. M., Liu, H., MacDonald, A. B., McComiskey,
983 A., Moore, R., Painemal, D., Russell, L. M., Seinfeld, J. H., Shook, M., Smith, W. L., Thornhill, K., Tselioudis,
984 G., Wang, H., Zeng, X., Zhang, B., Ziemba, L., and Zuidema, P.: Aerosol–cloud–meteorology interaction airborne
985 field investigations: Using lessons learned from the U.S. west coast in the design of ACTIVATE off the U.S. East
986 Coast, *Bulletin of the American Meteorological Society*, 100, 1511-1528, [https://doi.org/10.1175/BAMS-D-18-](https://doi.org/10.1175/BAMS-D-18-0100.1)
987 [0100.1](https://doi.org/10.1175/BAMS-D-18-0100.1), 2019.

988 Sorooshian, A., Alexandrov, M. D., Bell, A. D., Bennett, R., Betito, G., Burton, S. P., Buzanowicz, M. E., Cairns, B.,
989 Chemyakin, E. V., Chen, G., Choi, Y., Collister, B. L., Cook, A. L., Corral, A. F., Crosbie, E. C., van Dierenhoven,
990 B., DiGangi, J. P., Diskin, G. S., Dmitrovic, S., Edwards, E. L., Fenn, M. A., Ferrare, R. A., van Gilst, D., Hair, J.
991 W., Harper, D. B., Hilario, M. R. A., Hostetler, C. A., Jester, N., Jones, M., Kirschler, S., Kleb, M. M., Kusterer,
992 J. M., Leavor, S., Lee, J. W., Liu, H., McCauley, K., Moore, R. H., Nied, J., Notari, A., Nowak, J. B., Painemal,
993 D., Phillips, K. E., Robinson, C. E., Scarino, A. J., Schlosser, J. S., Seaman, S. T., Seethala, C., Shingler, T. J.,
994 Shook, M. A., Sinclair, K. A., Smith Jr, W. L., Spangenberg, D. A., Stamnes, S. A., Thornhill, K. L., Voigt, C.,
995 Vömel, H., Wasilewski, A. P., Wang, H., Winstead, E. L., Zeider, K., Zeng, X., Zhang, B., Ziemba, L. D., and
996 Zuidema, P.: Spatially coordinated airborne data and complementary products for aerosol, gas, cloud, and
997 meteorological studies: the NASA ACTIVATE dataset, *Earth Syst. Sci. Data*, 15, 3419-3472,
998 <https://doi.org/10.5194/essd-15-3419-2023>, 2023.

999 Stahl, C., Cruz, M. T., Bañaga, P. A., Betito, G., Braun, R. A., Aghdam, M. A., Cambaliza, M. O., Lorenzo, G. R.,
1000 MacDonald, A. B., Hilario, M. R. A., Pabroa, P. C., Yee, J. R., Simpas, J. B., and Sorooshian, A.: Sources and
1001 characteristics of size-resolved particulate organic acids and methanesulfonate in a coastal megacity: Manila,
1002 Philippines, *Atmospheric Chemistry and Physics*, 20, 15907-15935, <https://doi.org/10.5194/acp-20-15907-2020>,
1003 2020.

1004

1005 Stevens, B., Cotton, W. R., Feingold, G., and Moeng, C.-H.: Large-eddy simulations of strongly precipitating, shallow,
1006 stratocumulus-topped boundary layers, *Journal of the Atmospheric Sciences*, 55, 3616-3638,
1007 [https://doi.org/10.1175/1520-0469\(1998\)055<3616:LESOSP>2.0.CO;2](https://doi.org/10.1175/1520-0469(1998)055<3616:LESOSP>2.0.CO;2), 1998.

1008 Su, T., Zheng, Y., and Li, Z.: Methodology to determine the coupling of continental clouds with surface and boundary
1009 layer height under cloudy conditions from lidar and meteorological data, *Atmos. Chem. Phys.*, 22, 1453-1466,
1010 <https://doi.org/10.5194/acp-22-1453-2022>, 2022.

1011 Thornhill, K. L., Anderson, B. E., Barrick, J. D. W., Bagwell, D. R., Friesen, R., and Lenschow, D. H.: Air motion
1012 intercomparison flights during Transport and Chemical Evolution in the Pacific (TRACE-P)/ACE-ASIA. *Journal*
1013 *of Geophysical Research: Atmospheres*, 108, D20, <https://doi.org/10.1029/2002JD003108>, 2003.

1014 Tornow, F., Ackerman, A. S., Fridlind, A. M., Cairns, B., Crosbie, E. C., Kirschler, S., Moore, R. H., Painemal, D.,
1015 Robinson, C. E., Seethala, C., Shook, M. A., Voigt, C., Winstead, E. L., Ziemba, L. D., Zuidema, P., and
1016 Sorooshian, A.: Dilution of boundary layer cloud condensation nucleus concentrations by free tropospheric
1017 entrainment during marine cold air outbreaks. *Geophysical Research Letters*, 49, e2022GL098444,
1018 <https://doi.org/10.1029/2022GL098444>, 2022.

1019 Twomey, S.: Pollution and the planetary albedo, *Atmospheric Environment* (1967), 8, 1251-1256,
1020 [https://doi.org/10.1016/0004-6981\(74\)90004-3](https://doi.org/10.1016/0004-6981(74)90004-3), 1974.

1021 Wang, Z., Mora Ramirez, M., Dadashazar, H., MacDonald, A. B., Crosbie, E., Bates, K. H., Coggon, M. M., Craven,
1022 J. S., Lynch, P., Campbell, J. R., Azadi Aghdam, M., Woods, R. K., Jonsson, H., Flagan, R. C., Seinfeld, J. H.,
1023 and Sorooshian, A.: Contrasting cloud composition between coupled and decoupled marine boundary layer
1024 clouds, *Journal of Geophysical Research: Atmospheres*, 121, 11,679-611,691,
1025 <https://doi.org/10.1002/2016JD025695>, 2016.

1026 Warren, S.G., Hahn, C.J., London, J., Chervin, R.M., Jenne, R.L.: Global distribution of total cloud cover and cloud
1027 type amounts over the ocean. United States: n. p., <https://doi.org/10.2172/5415329>, 1988.

1028 Ziemba, L. D., Lee Thornhill, K., Ferrare, R., Barrick, J., Beyersdorf, A. J., Chen, G., Crumeyrolle, S. N., Hair, J.,
1029 Hostetler, C., Hudgins, C., Obland, M., Rogers, R., Scarino, A. J., Winstead, E. L., and Anderson, B. E.: Airborne
1030 observations of aerosol extinction by in situ and remote-sensing techniques: Evaluation of particle hygroscopicity.
1031 *Geophysical Research Letters*, 40, 2, 417-422, <https://doi.org/https://doi.org/10.1029/2012GL054428>, 2013.

1032 Zuidema, P., Painemal, D., de Szoek, S., and Fairall, C.: Stratocumulus cloud-top height estimates and their climatic
1033 implications, *Journal of Climate*, 22, 4652-4666, <https://doi.org/10.1175/2009JCLI2708.1>, 2009.